An extended calibration of the olivine–spinel aluminum exchange thermometer: Application to the melting conditions and mantle lithologies of large igneous provinces

Yishen Zhang[1,*], Olivier Namur[1], Weiran Li[2,3], Oliver Shorttle[2], Esteban Gazel[4], Eleanor Jennings[5], Peter Thy[6], Timothy L. Grove[7], Bernard Charlier[8]

[1] Department of Earth and Environmental Sciences, KU Leuven, 3000 Leuven, Belgium

[2] Department of Earth Sciences, University of Cambridge, Cambridge, UK

[3] Department of Earth Sciences, University of Hong Kong, Hong Kong, China

[4] Department of Earth and Atmospheric Sciences, Cornell University, Ithaca, NY, USA

[5] Department of Earth and Planetary Sciences, Birkbeck, University of London, Malet Street, London WC1E 7HX, United Kingdom

[6] Department of Earth and Planetary Sciences, University of California, Davis, CA 95616, USA

[7] Department of Earth, Atmospheric and Planetary Sciences, Massachusetts Institute of Technology, 77 Massachusetts Avenue, Cambridge, 02139 Massachusetts, USA

[8] Department of Geology, University of Liège, 4000 Sart Tilman, Belgium

* Corresponding author. E-mail address: yishen.zhang@kuleuven.be

27 **ABSTRACT**

28 The application of the olivine–spinel aluminum exchange thermometer to natural samples is

29 limited by the restricted experimental dataset on which it was calibrated. Here, we present a

30 new dataset of 46 high-temperature crystallization experiments and 21 reanalyzed published

31 experiments, which we used to extend the calibration to higher and lower temperatures. The

32 final calibration dataset spans a range of conditions relevant to crustal and upper mantle

33 processes: 1174–1606 °C, 0.1–1350 MPa, QFM−2.5 to QFM+7.2 (oxygen fugacity, fO$_2$,

34 reported in log units relative to the quartz–fayalite–magnetite buffer, QFM), and 0–7.4 wt.%

35 H$_2$O$_{melt}$. We propose three new models. The first is thermodynamically self-consistent,

36 based on spinel Fe, Mg, Al, and Cr compositions and Al exchange between olivine and

37 spinel. The second and third are empirical models that consider fewer elemental exchanges:

38 the second uses only Al exchange and spinel compositions, whereas the third considers

39 olivine–spinel Al and Cr exchange. All models include the modest effect of pressure on

40 olivine-spinel equilibrium chemistry, whereas fO$_2$ and water content have negligible effects.

41 In general, as fewer elements are considered in the olivine–spinel exchange, the fit to

42 experimental data worsens. Conversely, the associated decrease in model complexity

43 improves their robustness against systematic errors when applied to natural crystal pairs: the

44 thermodynamic model may underestimate crystallization temperatures in natural samples

45 due to spinel subsolidus re-equilibration, whereas the empirical models (independent of Fe

46 and Mg in spinel) are less sensitive to re-equilibration but yield temperatures with larger

47 uncertainties. We applied a statistical test to select the most appropriate model for

48 application to natural samples. When applied to lavas from mid-ocean ridges, Iceland, Skye,

49 Emeishan, Etendeka, and Tortugal, our new temperature estimates are 30–100 °C lower than

50 previously proposed. The lower temperature estimates cause a lower mantle melting

51 temperature and significant impacts on the mantle lithology constraints.

52 **Keywords:** Cr-spinel; Large igneous province; Mantle melting; Olivine; Thermometry

53

DATA AVAILABILITY

54   **DATA AVAILABILITY**

55   Additional data is available as supplementary electronic files. All calculations of each model,

56   the protocol to choose the results are written in a python script and Excel spreadsheet

57   (https://github.com/eazzzon/olspthermo).

67

INTRODUCTION

In the mantle, convection and upwelling plumes generate substantial magma volumes in mid-ocean ridge (MOR) systems and can produce oceanic or continental large igneous provinces (LIPs; e.g., Morgan, 1971; White & McKenzie, 1989; Campbell & Griffiths, 1990). Buoyantly ascending plume materials melt at relatively shallow depths (Sleep, 1992, 1996), eventually producing large volumes of magma through decompression melting of the plume head. Mantle plumes are sustained by temperature-induced density differences (e.g., Rayleigh-Taylor instability) compared to the ambient mantle (White & McKenzie, 1995), and large thermal anomalies (ca. 100–200 °C; White & McKenzie, 1989) are generally considered requisite for LIP activity. This thermal anomaly is commonly expressed as the excess temperature (T_{ex}), which is the difference between the mantle potential temperature (T_p, the mantle temperature extrapolated along the adiabat at 1 bar without melting; McKenzie & Bickle, 1988) at hotspots and of the ambient mantle (i.e., average MORs, $T_p \approx$ 1330 °C; e.g., Green & Falloon, 2005; Falloon et al., 2007), where melts are generated by near-adiabatic upwelling of the upper mantle (McKenzie & Bickle, 1988).

The temperatures of LIP mantle sources have often been estimated by applying olivine-liquid geothermometers (Beattie, 1993; Putirka, 2005, 2008) to picritic basalts containing forsteritic olivine (forsterite content expressed as Fo = 100 × molar Mg/[Mg + Fe]) to calculate the olivine-melt equilibrium temperature and then T_p (Putirka et al., 2007). Other approaches involve modeling mantle melting as a function of pressure and temperature and comparing the modeled primary magmas with those determined from natural (near-) primary melts (Ghiorso & Sack, 1995; Ghiorso et al., 2002; Herzberg & Asimow, 2015; Brown Krein et al., 2021). However, these models require assumptions of primary melt compositions, even though near-primary melts rarely erupt (O'Hara, 1968; Neave et al., 2019; Neave & Namur, 2022). Therefore, primary melt compositions are usually estimated by adding or subtracting an olivine component iteratively based on olivine-melt Fe-Mg exchange until equilibrium with a mantle Fo target is attained, often

4

95　　leading to large uncertainties in the FeO and MgO contents of the calculated primary melt

96　　(e.g., Herzberg *et al.*, 2007).

97　　　　The olivine-spinel aluminum exchange thermometer (hereafter OSAT; Wan *et al.*,

98　　2008; Coogan *et al.*, 2014) is based on the exchange of Al between olivine and spinel,

99　　written as $K_{D_{Al}} = [Al_2O_3]_{Ol}/[Al_2O_3]_{Spl}$ (Al_2O_3 concentrations in wt.%). This thermometer

100　　obviates the need to assume a melt composition because it determines the crystallization

101　　temperature directly from the equilibrium compositions of olivine and coexisting spinel.

102　　However, the OSAT was only calibrated at low pressure (0.1 MPa) and a restricted range of

103　　dry melt compositions (SiO_2: 40.5–45.9 wt.%, MgO: 17.5–23.5 wt.%, FeO: 10.6–12.2 wt.%,

104　　Al_2O_3: 9.0–15.4 wt.%), olivine compositions (Fo_{86-100}), spinel compositions (Cr# = 0–0.69,

105　　where Cr# = molar Cr/[Cr + Al]), and oxygen fugacities (fO_2 = QFM−1.5 to QFM+0.5, with

106　　70% of the experiments performed at QFM−1.5; QFM indicates the quartz–fayalite–

107　　magnetite equilibrium). Therefore, its applicability in diverse geological settings,

108　　particularly those with Cr-rich spinel in equilibrium with Fo-rich olivine, is questionable; it

109　　is unknown how intensive parameters such as pressure, fO_2, and volatile contents affect the

110　　OSAT calibration.

111　　　　In this study, we performed and analyzed new experiments, reanalyzed prior

112　　experiments, and combined our results with the high-quality measurements of Wan *et al.*

113　　(2008) and Coogan *et al.* (2014) to extend the OSAT calibration. Our final experimental

114　　database spans 0.1–1350 MPa, 1174–1606 °C, and QFM−2.5 to QFM+7.2 (i.e., air), and

115　　includes three hydrous experiments containing 3.7–7.4 wt.% H_2O_{melt}.

116　　　　We also developed a thermodynamic formalism to better understand olivine–spinel

117　　Al exchange. Our model suggests that, besides $K_{D_{Al}}$ and spinel Cr#, other components

118　　involving Fe and Mg in spinel have a significant impact on the calculated olivine–spinel

119　　equilibrium temperature and therefore on the previous OSAT calibration. This model is

120　　expected to be the most accurate parameterization for olivine and spinel compositions that

121　　quenched rapidly, inhibiting Mg–Fe exchange during cooling. However, this comprehensive

5

122   thermodynamic model may retrieve systematically low temperature estimates when applied

123   to natural rocks due to subsolidus olivine–spinel Fe–Mg re-equilibration. Therefore, we also

124   report two empirical expressions that may be less prone to underestimating olivine–spinel

125   equilibration temperatures in variably re-equilibrated natural samples, but are less precise

126   and accurate than the thermodynamic model. The first empirical model follows a similar

127   formalism as Coogan et al. (2014), only involving $K_{D_{Al}}$ and spinel Cr#. The second

128   incorporates the exchange of Cr between olivine and spinel ($K_{D_{Cr}}$ = $[Cr_2O_3]_{Ol}/[Cr_2O_3]_{Spl}$,

129   Cr_2O_3 concentrations in wt.%) which improves the accuracy of this model. We find that

130   pressure has a moderate impact on the temperature calculations in all models, whereas fO$_2$

131   and water have negligible effects.

132   We applied our new models to re-constrain the crystallization temperature for

133   published olivine-spinel pairs in natural rocks. A multi-component mantle melting model

134   (Phipps Morgan, 2001; Shorttle et $al.,$ 2014) is then applied to match crystallization

135   temperature with geochemical constraints to estimate mantle temperatures and mantle

136   lithology components (Matthews et $al.,$ 2016; 2021). Our results suggest that previous

137   studies using the model of Coogan et al. (2014) may have overestimated the crystallization

138   temperature of olivine by as much as ~30–100 °C for intra-plate LIPs, significantly

139   overestimating T_p and impacting constraints on the mantle lithology. Based on our results,

140   we provide new constraints on mantle melting conditions and mantle lithologies for MORs,

141   Iceland, Skye, and intra-plate LIPs including Emeishan, Etendeka, and Tortugal.

142

The olivine-spinel aluminum exchange thermometer (OSAT)

143

144   The OSAT (Wan et al., 2008; Coogan et al., 2014) determines the equilibrium temperature

145   of olivine-spinel pairs, which corresponds to the minimum saturation temperature of these

146   two phases near the liquidus of their primitive parental melts (e.g., Jennings et al., 2019).

147   The crystallization temperature is calculated based on the concentration (in wt.%) of Al_2O_3

148   in olivine and those of Al_2O_3 and Cr_2O_3 in spinel as:

6

$$T\ (K) = \frac{10,000}{0.575(0.162) + 0.884(0.043)\ Cr\# - 0.897(0.025)\ \ln(K_{D_{Al}})} \quad (1)$$

149 with the standard errors on the determined coefficients reported in parentheses. The slow

150 diffusion rate of Al_2O_3 in olivine minimizes the effect of re-equilibration at low

151 temperatures (Spandler & O'Neil, 2010). The OSAT has been widely used to investigate the

152 temperature of formation of terrestrial and extraterrestrial magmas (Gavrilenko *et al.*, 2016;

153 Prissel *et al*., 2017; Trela *et al*., 2017; Goltz *et al.,* 2020; Jennings *et al*., 2020; Matthews *et*

154 *al*., 2021; Ramsey *et al*., 2021;), including those of LIPs. However, the model has faced

155 criticism for the limited experimental database used for its calibration, which has limited its

156 application. The main issues with the previous calibration are: (1) the range of experimental

157 spinel compositions is quite narrow compared to those observed in natural rocks (see next

158 subsection); (2) the highest experimental temperature in the database (1450 °C) is

159 significantly lower than magmatic temperatures calculated in many natural settings

160 (>1500 °C; e.g., komatiite, Trela *et al*., 2017; LIPs, Matthews *et al*., 2021; Martian

161 shergottites, Ramsey *et al*., 2021), implying that the currently available expression must be

162 extrapolated beyond its calibration range; and (3) high-pressure and hydrous experiments

163 are absent in the calibration database.

164

165 **Comparison of the original calibration experiments with natural rocks**

166 To demonstrate the limitations of the existing olivine–spinel aluminum exchange calibration,

167 we compare the olivine and spinel compositions used in the calibration experiments to those

168 most common in LIPs.

169 To compare spinel compositions, we used the ternary projection of the spinel prism, Al–Cr–

170 Fe^{3+} (Fig. 1a). Spinel Fe^{3+} contents were calculated by charge balance on a four-oxygen

171 basis (Droop, 1987). Both experimental and natural spinel compositions show a dominant

172 trend from the Cr apex towards the Al apex. However, spinel in primitive basalts commonly

173 have compositions plotting far beyond the calibration range (Cr# = 0.23–0.85 in natural

174 spinel vs. 0–0.69 in the calibration experiments; Fig. 1b). Natural spinel also has higher Fe^{3+}

7

175   contents and occasionally higher TiO_2 contents (>5 wt.%; Fig. 1c) compared to the

176   calibration dataset. Therefore, the experimental spinel compositions are only directly

177   comparable to MORB compositions and partially overlap those from Iceland. The chemical

178   composition of igneous spinel is known to be a complex function of intensive parameters

179   (pressure, temperature, fO_2) and melt composition (Katsura & Ito, 1989; Ballhaus *et al*.,

180   1991; Ariskin & Nikolaev, 1996; Kamenetseky *et al.,* 2001). The chemical differences

181   between experimental spinel compositions in the calibration dataset and natural spinel may

182   be due to the narrow fO_2 range and/or restricted melt compositions used in the experiments;

183   many of the experiments were performed in the Cr-free simplified $CaO–MgO–Al_2O_3–SiO_2$

184   (CMAS) system, with pure spinel in equilibrium with forsterite. However, the observed

185   differences could also be partly related to subsolidus Fe-Mg re-equilibration between olivine

186   and spinel in natural rocks.

187   Figure 2 compares olivine Al_2O_3 and Cr_2O_3 concentrations as a function of Fo

188   content. The restricted experimental conditions also limited the range of experimental

189   olivine compositions to $Fo_{86–100}$ (Fo_{100} crystalized in CMAS experiments), compared to the

190   much wider range observed in natural olivine ($Fo_{68–94}$, Fig. 2). The Al_2O_3 (190–1,519 µg/g)

191   and Cr_2O_3 (165–3,420 µg/g) contents of natural olivine crystals also commonly fall outside

192   the calibration interval (Al_2O_3, 450–1,686 µg/g; Cr_2O_3, 45–2,990 µg/g).

193

194   **EXPERIMENTAL STRATEGY AND ANALYTICAL METHODS**

195   **Selection and preparation of starting materials**

196   To co-saturate olivine and spinel at different temperatures from a wide range of melt

197   compositions, we used a variety of natural and synthetic starting compositions with 10.1–

198   34.9 wt.% MgO, 38.0–50.2 wt.% SiO_2, 3.8–16.3 wt.% Al_2O_3, 0.2–6.0 wt.% total alkalis

199   ($Na_2O + K_2O$) and 0.1–2.0 wt.% Cr_2O_3. Details of the different starting compositions are

200   reported in Table 1 and summarized here.

201   1) We used two komatiitic compositions from the Tortugal lava suite, Costa Rica: TO-

202   080514-1 and TO-080514-2 (Trela *et al*., 2017), here abbreviated as TO1 and TO2,

8

203   respectively. These lavas have >33 wt.% MgO, different TiO_2 contents (TO1: 0.79

204   wt.%; TO2: 0.89 wt.%) and preserve olivine with high-Cr# spinel inclusions

205   (Cr# >0.85).

206 2) Five basaltic compositions cover a range of melt SiO_2 (38.0–50.2 wt.%,) and Al_2O_3

207   contents (3.8–16.3 wt.%), which may affect the exchange of Al between the liquid,

208   olivine, and spinel (Evans *et al*., 2008; Hanson & Jones, 1998). These five

209   compositions include: primitive basalts from Pico, Azores (PI052, van Gerve *et al.,*

210   2021) and Osorno volcano, Chile (OS082; Bechon *et al*., 2022); two alkali-rich (>5

211   wt.%), SiO_2-undersaturated basalts from Nyiragongo volcano, DR Congo (Ny17-

212   135 and Ny17-161, Molendijk *et al*., 2023a); and a porphyritic basalt from the

213   Nyamuragira volcano, DR Congo (NYA2012-09-018, here abbreviated as NYAM).

214 3) We prepared three synthetic compositions as analogues to TO1, TO2, and Ny17-135

215   (Table 1). The objective here was to test the potential effect of relict olivine and

216   spinel grains in natural materials with liquidus temperatures too high to completely

217   melt in a standard muffle furnace prior to experimental runs in the vertical gas

218   mixing furnace (see Experimental methods, below).

219 4) Finally, we synthesized the starting composition of Wan *et al*. (2008; here named

220   2Cr'+1Cr) to check interlaboratory experimental reproducibility and test analytical

221   uncertainties under different analytical settings.

222   Natural samples were crushed to finer than 1 μm in a ball mill and melted three

223 times at >1500 °C in a Pt crucible in a muffle furnace: the first melting batch was used to

224 saturate the Pt crucible and was not kept; the two additional batches were used to ensure the

225 compositional homogeneity of the glass. The synthetic compositions were prepared from

226 mixtures of high-purity oxides and silicates (SiO_2, TiO_2, Al_2O_3, MnO, MgO, Fe_2O_3, $CaSiO_3$,

227 $AlPO_4$, Na_2SiO_3, $K_2Si_4O_9$, Cr_2O_3, NiO) in appropriate proportions. The silicates ($CaSiO_3$,

228 Na_2SiO_3, and $K_2Si_4O_9$) were prepared following Zhang *et al*. (2023).

229   Due to the dramatic increase of Cr_2O_3 solubility in the melt (>1 wt.%) at high

230 temperatures (>1450 °C; Borisova *et al*., 2020) and the potential increase of the Cr_2O_3

9

231   evaporation rate with increasing temperature (Sossi *et al*., 2019) in the gas mixing furnace,

232   most natural and all synthetic compositions were doped with 1–2 wt.% Cr_2O_3 (compositions

233   with 'Cr1' suffixes for 1 wt.% and 'Cr2' for 2 wt.% dopant, respectively; Table 1). In some

234   experiments, chromite and forsterite powders were added to change the liquidi of olivine

235   and spinel (Table 1). All starting powders were mixed and ground in ethanol for one hour

236   then dried at 120 °C before use in experiments.

237

238   **Experimental methods**

239   Experiments were conducted in a Nabertherm HTRV 50/150/17 vertical tube furnace at KU

240   Leuven, Belgium, or a GERO HTRV 70-250/18 vertical tube furnace at the University of

241   Liège, Belgium. Approximately 50 mg of starting material was suspended on a 0.2-mm-

242   diameter Pt loop. To avoid potential Fe loss, the Pt loops were pre-saturated with the

243   experimental material for ~24 h at the same temperature and fO$_2$ to be used in the

244   experiment, then cleaned with HF. Prior to experiments, all sample pellets were briefly

245   heated in a muffle furnace at 1550 °C to ensure sintering. Experimental samples were then

246   suspended for 7–120 h in the hot spot of the vertical furnace (~5 cm in height, where

247   temperature is stable to within ±3 and ±1 °C in the Nabertherm HTRV 50/150/17 and

248   GERO HTRV 70-250/18 furnaces, respectively). Temperature was measured using a S-type

249   (Pt–Pt$_{90}$Rh$_{10}$) thermocouple calibrated against the melting points of Ag and Au. Oxygen

250   fugacity was controlled using mixtures of high-purity CO and CO_2 flushed upward from the

251   bottom of the alumina ceramic furnace tube. Bronkhorst gas-flow controllers were used to

252   set the flow rate at 0.12 cm/s. The accuracy on the fO$_2$ was checked with a zirconia oxygen

253   sensor. Because it is challenging to produce large spinel and olivine crystals above 1500 °C,

254   in experiments at such high temperatures, the temperature was first oscillated by ±10 °C for

255   ~1–2 h to increase the sizes of olivine and spinel crystals before holding the experiments

256   isothermally for the remainder of the experiment. All experiments were drop-quenched in

257   water. Experimental run conditions are detailed in Table 2.

10

Selection of previous experiments

To expand the experimental database and test the effects of pressure and water content on

the Al exchange between olivine and spinel, we also selected and reanalyzed 21 published

experiments, including crystallization experiments on Munro komatiite, Canada (Thy, 1995),

lunar magma ocean (Charlier *et al.,* 2018), harzburgite melting experiments (Parman &

Grove, 2004), hydrous melting experiments on komatiite from Commondale Ultramafic

Suite, South Africa (Barr et al., 2009), and melting experiments on fertile mantle component

(Mitchell & Grove, 2015). These experiments span a range of temperature between 1215

and 1350 °C, pressure between 0.1 and 1350 MPa, fO_2 from QFM−2.5 to QFM, and between

0 and 7.4 wt.% H_2O_{melt}.

Analytical methods

Analyses were performed using a JEOL JXA-8530F Wavelength Dispersive Spectrometer

(WDS) Field Emission Gun Electron probe micro-analyzer (EPMA) at the Department of

Material Engineering, KU Leuven, Belgium, and a Cameca SX-100 Electron Microprobe at

the Department of Earth Sciences, University of Cambridge. Major and trace elements were

measured with different calibrations and analytical setups detailed in the Supplementary

data and summarized here. Major element concentrations in olivine and spinel were

generally within 98% accuracy of the reference values.

Experimental products were mounted in high-purity epoxy and polished for analysis.

Electron probe micro-analyzer measurements of trace elements in olivine, especially Cr and

Al, are known to suffer from secondary fluorescence from surrounding spinel or melt

(Llovet *et al*., 2012, Gavrilenko *et al*., 2023; Llovet *et al*., 2023). We used FANAL (Llovet

et al., 2012) and PENEPMA (Llovet & Salvat, 2017), Monte Carlo simulation tools to

model coupled electron-photon transportation, and simulated analyses of San Carlos olivine

and VG-2 glass standards. The results show that measuring olivine compositions at least 5

μm (based on FANAL) and 15 μm (based on PENEPMA) inward from the phase margin

dramatically reduces the influence of secondary fluorescence (Fig. S1). This analytical

11

286   strategy was applied to sufficiently large olivine (> 10 μm) crystals in the experimental

287   charges. Analytical results for experiments with smaller olivine (~ 10 μm) were manually

288   filtered by removing anomalous outliers (see more details below).

289   At KU Leuven, Al, P, Cr, and Ca in olivine were measured with a focused beam operating at

290   20 kV and 300 nA and calibrated with a MongOl sh11-2 olivine (Batanova *et al*., 2019).

291   Detection limits were 6 μg/g for Al_2O_3, 9 μg/g for P_2O_5, and 4 μg/g for Cr_2O_3. High-

292   precision wavelength scanning at 20 kV and 300 nA was performed prior to each session to

293   accurately determine the Al, Cr, and P peak positions (Fig. S2). Background positions were

294   chosen near (~0.5 mm) the base of the peak to minimize the subtraction of background

295   counts (Batanova *et al*., 2015). Because it is difficult to properly analyze major elements by

296   WDS at high beam currents due to the high counting rates and the possibility of

297   oversaturating the detectors, Si, Mg, and Fe in olivine and all elements in spinel were

298   measured afterwards with a focused beam at 15 kV and 20 nA and calibrated with natural

299   and synthetic primary standards (see Supplementary data). To ensure reproducibility

300   between sessions, secondary standards (San Carlos olivine NMNH 111312-44 for olivine,

301   chromite NMNH 117075 for spinel) were analyzed at regular intervals to correct for any

302   instrumental drift. In the San Carlos olivine, we measured 338 ± 14 μg/g Al_2O_3 (1σ, $n = 72$),

303   43 ± 22 μg/g P_2O_5 (1σ), and 135 ± 9 μg/g Cr_2O_3 (1σ), which are comparable with the results

304   of Batanova *et al*. (2015; 330 ± 10 μg/g Al_2O_3, 50 ± 10 μg/g P_2O_5, 152 ± 8 μg/g Cr_2O_3,

305   uncertainties in 2σ). Glasses were analyzed at KU Leuven using a beam defocused to 10–30

306   μm diameter and operating at 15 kV and 10 nA. Quench textures were observed in the

307   highest temperature experiments (>1500 °C), which causes MgO depletion in the interstitial

308   melt. For those experiments, melt compositions were measured on mixtures of melt and

309   quenched crystals, increasing the 1σ standard deviations for melt MgO and FeO contents to

310   1.0–4.7 wt.% and 0.4–1.3 wt.%, respectively. Glass secondary standards NMNH 111312-44,

311   VG2, and GOR 132-G (Jochum *et al*., 2006) were analyzed at regular intervals, and the

312   results were again within 98% accuracy of the reference values (see supplementary dataset).

12

313   X-ray compositional maps were acquired following the procedure of Shea *et al.* (2019), but

314   using a 20 kV and 300 nA electron beam.

315   At the University of Cambridge, we followed a similar procedure using a focused

316   beam operating at 15 kV and 100 nA beam to measure Al, Cr, and P in olivine. Detection

317   limits were 28 µg/g for Al_2O_3, 117 µg/g for P_2O_5, and 87 µg/g for Cr_2O_3. We used the

318   MongOl sh11-2 olivine ($n = 8$) as a secondary standard and obtained 487 ± 10 µg/g Al_2O_3

319   (1σ), 228 ± 40 µg/g P_2O_5 (1σ), and 209 ± 20 µg/g Cr_2O_3 (1σ), again consistent with the

320   reference values (463 ± 18 µg/g Al_2O_3, 152 ± 8 µg/g P_2O_5, 182 ± 6 µg/g Cr_2O_3, uncertainties

321   in 2σ; Batanova *et al.*, 2019).

322

323   **Interlaboratory experimental and analytical uncertainties**

324   To calibrate our extended OSAT with as many relevant experiments as possible, we chose to

325   include the experimental results of Wan *et al.* (2008) and Coogan *et al.* (2014), which we

326   could not reanalyze for this study. It is therefore important to critically assess whether we

327   can reproduce their phase equilibria observations and reproduce their chemical

328   measurements, including minor elements such as Al in olivine. Therefore, we reproduced

329   two experiments from Wan *et al.* (2008): w83 (~QFM−1.6, 1250 °C), reproduced here in

330   experiment NAB89U, and w71 (~QFM−1.6, 1300 °C), reproduced here in experiment

331   NAB90U. We chose these two relatively low-temperature experiments because it is more

332   challenging to attain equilibrium under those conditions.

333   Experiments NAB89U and NAB90U produced phase equilibria (liquid, olivine, and

334   spinel) and compositions similar to those reported by Wan *et al.* (2008). Importantly,

335    $\ln(K_{D_{Al}})$ values were almost identical: -6.16 ± 0.04 (1σ, uncertainty calculated from error

336   propagation with a Monte Carlo algorithm) in NAB89U vs. -6.14 ± 0.05 (1σ) in w83, and

337   -5.80 ± 0.03 (1σ) in NAB90U vs. -5.90 ± 0.05 (1σ) in w71. Spinel compositions were also

338   identical: Fe^{3+}/Fe^{2+} in spinel was 0.16 ± 0.05 (1σ) in NAB89-U vs. 0.17 ± 0.09 (1σ) in w83,

339   and 0.21 ± 0.03 (1σ) in NAB90-U vs. 0.21 ± 0.07 (1σ) in w71. This suggests that

13

340   interlaboratory analytical and experimental uncertainties are minor, and further that we can

341   include the published experimental results from Wan *et al*. (2008) and Coogan *et al*. (2014)

342   in our new OSAT calibration database. This also suggests that our experiments attained

343   equilibrium (see next subsection).

344

345   **Attainment of equilibrium**

346   The attainment of equilibrium between melt, olivine, and spinel, especially for slowly

347   diffusing minor elements, is critical to our study. The considerably long durations of our

348   experimental runs (7–120 h), most much longer than in high-temperature experiments in the

349   previous calibration (Wan *et al*., 2008) or other high-temperature experimental studies (e.g.,

350   Tuff *et al*., 2005; Matzen *et al*., 2011; Krasheninnikov *et al*., 2017; Koshlyakova *et al.*,

351   2022), were chosen to ensure that equilibrium was attained. We note that a few high-

352   temperature experiments (>1500 °C, Table 2) lasted only a few hours (≥7 h), but that the

353   fast elemental diffusion at such high temperatures and the low crystallinity of those

354   experiments suggest that equilibrium was attained even in those shorter runs.

355   We also evaluated the attainment of equilibrium based on compositional and

356   textural characteristics. Olivine and spinel were generally euhedral, suggesting they formed

357   at equilibrium. The experimental charges also show homogeneous backscattered electron

358   intensities for melts and minerals (Fig. 3). Fe-Mg partition coefficients between olivine and

359   melt ($K_{D_{Fe-Mg}}^{Ol-melt}$) range from 0.26 to 0.34 (see in the Supplementary data), consistent with

360   previous experiments (e.g., Roeder & Emslie, 1970; Toplis & Carroll, 1995) and

361   thermodynamic models (e.g., Toplis, 2005; Blundy *et al*., 2020). In general, $K_{D_{Fe-Mg}}^{Ol-melt}$ is

362   positively correlated with the melt SiO_2 content, which supports the impact of melt silica

363   activity on Fe-Mg exchange between olivine and melt (Gee & Sack, 1988; Toplis, 2005;

364   Koshlyakova *et al.*, 2022). In particular, experiments using silica-undersaturated and alkali-

365   rich compositions have $K_{D_{Fe-Mg}}^{Ol-melt} < 0.27$ (0.22–0.26), consistent with experimental results

366   on similar compositions (Gee & Sack, 1988; Molendijk *et al*., 2023b). In contrast, high-

14

367 temperature experiments with quench textures occasionally have $K_{\mathrm{D}\,\mathrm{Fe-Mg}}^{\mathrm{Ol-melt}} = 0.34\text{–}0.35$,

368 beyond the range 0.30 ± 0.03; such high values may have resulted from analytical

369 heterogeneity due to the glass analyses involving mixtures of quench crystals and interstitial

370 melt (Mitchell & Grove, 2015).

371   Trace element (Al, P, Cr) partitioning in olivine may be affected due to the

372 formation of a boundary layer enrichment during initially rapid crystal growth (e.g., Shea *et*

373 *al*., 2019; Lang *et al*., 2022). This means that the above indicators of equilibrium (Fe-Mg

374 exchange and textural constraints) may not reflect trace element equilibration. Therefore, we

375 measured rim-to-core profiles comprising 6−7 spot analyses (ca. 5–6 μm spacing) per

376 profile in one olivine crystal from each experiment to check the homogeneity of their trace

377 element distributions. The profiles generally show very small deviations (~50 μg/g, 1σ) for

378 Al_2O_3 and even less variability for other trace elements (see Supplementary material,

379 Section 2). We also acquired EPMA X-ray compositional maps of experiments treated with

380 thermal oscillation and experiments that were run at more than 200 °C below their liquidi.

381 Chemical maps do not show any apparent P, Al, or Cr zoning (see Supplementary material,

382 Section 2). Relict phases were occasionally observed in the cores of olivine crystals in

383 experiments performed on compositions with high liquidus temperatures. The uniform

384 compositions of the crystal rims, however, suggest that the early disequilibrium did not

385 preclude the attainment of equilibrium between the outer part of the crystals and the adjacent

386 melt. Experiments conducted at more than 300 °C below the liquidus typically produced

387 small olivine crystals (~10 μm in length) with dendritic P and Al zoning patterns. These

388 experiments also produce olivine populations with distinct high and low Al_2O_3

389 concentrations; we used the low-concentration population in this study because it may

390 represent relaxation and equilibration during equilibrium crystal growth (Shea *et al*., 2019).

391

392 **RESULTS**

393 **Experimental results**

15

394   All reported experiments contain melt, olivine, and spinel. Four experiments performed at

395   more than 300 °C below the liquidus also contain clinopyroxene. Compositions of the

396   phases are given in supplementary dataset (Table S1).

397

398   *Melt*

399   Melt compositions are plotted as functions of MgO (in wt.%) and temperature in Figs. 4 and

400   S3, respectively. The experimental melts span a wide range of compositions, with 7.0–31.5

401   wt.% MgO, 38.9–54.6 wt.% SiO_2, 6.0–12.8 wt.% FeO, 3.9–17.3 wt.% Al_2O_3, 0.0–0.9 wt.%

402   Cr_2O_3, and 0.1–4.6 wt.% $Na_2O + K_2O$. Melt Al_2O_3 contents are anticorrelated with melt

403   MgO content, whereas melt Cr_2O_3 contents are positively correlated with melt MgO content

404   and temperature, consistent with the higher solubility of Cr_2O_3 in the melt at higher

405   temperature (Borisova *et al*., 2020).

406

407   *Olivine*

408   Olivine crystals are euhedral and ranged in size from ~10 μm to >100 μm (Fig. 3). Olivine

409   Fo contents range from Fo_{84} to Fo_{96} (Fig. 2). Minor and trace elements span a wide

410   compositional range: 0.1–1.3 wt.% CaO, 362–2118 μg/g Al_2O_3, 411–3706 μg/g Cr_2O_3, and

411   below the detection limit to 511 μg/g P_2O_5. Al_2O_3 and Cr_2O_3 contents are weakly correlated

412   with Fo content (Fig. 2). Olivine Cr_2O_3 content is positively correlated with melt Cr_2O_3

413   content (Fig. S4b). A broad positive correlation is also observed between olivine and melt

414   CaO contents (Fig. S4c), and the highest olivine CaO contents occur in experiments on

415   SiO_2-undersaturated compositions, consistent with previous findings (Gee & Sack, 1988;

416   Molendijk *et al*., 2023b). No correlation is apparent between olivine and melt Al_2O_3 or P_2O_5

417   contents (Fig. S4a, d, respectively).

418

419   *Spinel*

420   Spinel crystals range in size from ~1 μm to ~40 μm (Fig. 3). Spinel compositions are shown

421   in Figs. 1 and in Fig. S5 as functions of melt composition. Spinel Cr# ranges from 0.40 to

16

422   0.88, Mg# [= molar Mg/(Mg + Fe^{2+})] from 0.59 to 0.91, Fe^{3+}/Fe^{2+} from 0.08 to 2.48, the

423   ratio of Fe^{3+} to the sum of trivalent cations, $Fe^{3+}/(Fe^{3+} + Cr + Al)$, from 0.02 to 0.22, and

424   TiO_2 content from 0.5 to 5.5 wt.%. Experiments NAB01-F and NAB02-F, performed on

425   SiO_2-undersaturated and alkali-rich compositions, show the highest spinel TiO_2 contents (>5

426   wt.%), which correspond to the highest melt TiO_2 contents (>3 wt.%; Fig. S5). Spinel FeO

427   and Cr_2O_3 contents are only weakly correlated with melt FeO and Cr_2O_3 contents (Fig. S5).

428   A more significant correlation is observed between spinel and melt Al_2O_3 contents (Fig. S5),

429   consistent with previous observations (Borisova *et al.*, 2020; Sack & Ghiorso, 1991b;

430   Ariskin & Nikolaev, 1996; Poustovetov & Roeder, 2001).

431

432   **Summary of remeasured prior experiments**

433   Melt compositions in the reanalyzed published experiments and calibrations contain 8.4–

434   25.0 wt.% MgO, 42.0–55.6 wt.% SiO_2, 0–17.5 wt.% FeO, 8.3–21.6 wt.% Al_2O_3, and 0–0.54

435   wt.% Cr_2O_3. Olivine has Fo_{75-100} and contain 0–1.4 wt.% CaO, 183–1,686 μg/g Al_2O_3, 0–

436   2,990 μg/g Cr_2O_3, and 0–2,338 μg/g P_2O_5. Spinel has Cr# = 0–0.84, Mg# = 0.49–1,

437   Fe^{3+}/Fe^{2+} = 0.08–0.71, $Fe^{3+}/(Fe^{3+} + Cr + Al)$ = 0–0.17, and contains 0–1.38 wt.% TiO_2.

438

439   **Evaluating the model of Coogan *et al*. (2014)**

440   We assessed the OSAT of Coogan *et al*. (2014), which incorporates the earlier experiments

441   of Wan *et al*. (2008), by applying it to our updated experimental dataset (Fig. 5a). The

442   results show that the model of Coogan *et al*. (2014) significantly overestimated temperatures,

443   with a maximum deviation (ΔT [°C] = predicted temperature − measured temperature) of

444   197 °C, an average deviation of 44.7 ± 46.6 °C (1σ), and a root-mean-square error (RMSE)

445   of ±64.3 °C. These errors further demonstrate the need for a new calibration covering a

446   broader temperature range and accounting for additional factors affecting olivine–spinel Al

447   exchange, including spinel composition, fO_2, pressure, and melt H_2O content.

448

449   **REGRESSION AND THERMODYNAMIC MODELS**

17

450   To improve the reliability of the OSAT for natural samples, we here develop a

451   thermodynamic formalism for Al exchange between olivine and spinel and two empirical

452   regression models. We applied a Monte Carlo cross-validation (MCCV; e.g., Xu & Liang,

453   2001) algorithm to estimate the uncertainties of regression models.

454   **Regression strategy and models**

455   In our regression models, we first split the experimental dataset into a training dataset ($n =$

456   95) used for regression and a test dataset including 21 experiments not included in the

457   calibration to test the accuracy of the regression (details of training and test dataset are given

458   in the supplementary dataset, Tables S2, 3). The standard error estimation (SEE) on the

459   training dataset and RMSE on the test dataset were calculated accordingly. Then, to assess

460   model uncertainties and eliminate sampling bias, we used a MCCV algorithm. In each

461   calculation, we randomly divided the experimental dataset into a 5:1 ratio of training and

462   test datasets, and then performed 10-fold cross-validation on the training dataset to estimate

463   SEE_{MCCV} on the training dataset and then $RMSE_{MCCV}$ on the test dataset, which is also the

464   recommended error on the thermometric model. Detailed information on the training and

465   test datasets, as well as the MCCV results, are given in the Supplementary data (Tables S2

466   and S3; Section 3).

467

468   **Thermodynamic formalism**

469   To better understand the Al exchange between olivine and spinel, we here follow a

470   thermodynamic formalism. Coogan *et al*. (2014) argued that the most plausible mechanism

471   for incorporating Al into olivine in a Cr-spinel-bearing system is:

$$(MgAl^{TET})Al^{OCT}O_4^{Spl} = (MgAl^{TET})Al^{OCT}O_4^{Ol} \qquad (2)$$

472   which we follow in our thermodynamic framework (see details in Appendix A). For

473   simplicity, in the following we assume thermodynamic ideality in the incorporation of Al in

474   olivine, i.e., the excess energy caused from site ordering of Al is negligible. This assumption

475   is based on the following considerations: 1) trace element incorporation is usually

18

476 considered as a dilution so the internal energy can be calculated as a simplified pure

477 component (Ganguly, 2008); 2) to the best of the authors' knowledge, there are currently no

478 established models to accurately differentiate or calculate the coordination of different Al

479 species in olivine and no calibration for the interaction parameters between sites. Al may

480 also coordinate with a vacant site (Jollands *et al.*, 2018; Shea *et al.*, 2019; Lang *et al.*, 2022);

481 3) established thermodynamic models for other trace elements in olivine (e.g., Ni) with

482 similar assumption of ideality have shown a minimal influence on the internal energy (e.g.,

483 Matzen *et al.*, 2013). We therefore believe our thermodynamic framework remains valid

484 with this assumption. Al substitution in spinel is however more complicated due to its high

485 Al abundance, site ordering, and the known non-ideal mixing behavior of spinel components.

486 We apply the thermodynamic framework of Sack (1982) and Sack & Ghiorso (1991a,

487 1991b), and express the internal energy of spinel by five independent compositional

488 variables (X_i) (see details in Appendix A; Sack & Ghiorso, 1991b).

489 After organizing the thermodynamic framework, olivine–spinel Al exchange can be

490 described as (see Appendix A):

$$\ln\left(\frac{X_{Al_2O_3}^{Ol}}{X_{Mg^{2+}}^{TET} X_{Al^{3+}}^{OCT}}\right) + b = \frac{\varphi^{Spl}}{c_0 \times T} \tag{3}$$

491 which can be rearranged as:

$$T = \frac{\varphi^{Spl}}{c_0 \times \left(\ln\left(\dfrac{X_{Al_2O_3}^{Ol}}{X_{Mg^{2+}}^{TET} X_{Al^{3+}}^{OCT}}\right) + b\right)} \tag{4}$$

492

493 where:

19

$$\varphi^{\mathrm{Spl}} = c_1 X_2 + c_2 X_2^2 + c_3 X_2^{\frac{1}{2}}$$

$$+ c_4(1 - X_2)(1 + X_4 - X_2)$$

$$+ c_5(1 - X_2)(X_3) + c_6(1 - X_2)(X_4) + c_7(1 - X_2)(X_5)$$

$$+ c_8 X_3(X_3 + X_4 + X_5)$$

$$+ c_9 X_4(X_3 + X_4 + X_5)$$

$$+ c_{10} X_5(X_3 + X_4 + X_5)$$

$$- c_{11}(X_3)(X_4) - c_{12}(X_3)(X_5) - c_{13}(X_4)(X_5) + c_{14}$$

494   Here, R is the gas constant (8.314 J mol^{-1} K^{-1}), $X_{\mathrm{Mg}^{2+}}^{\mathrm{TET}}$ is the mole fraction of Mg in the

495   spinel tetrahedral site, $X_{\mathrm{Al}^{3+}}^{\mathrm{OCT}}$ is the mole fraction of Al in the spinel octahedral site, and T is

496   temperature in Kelvin. In Eq. 4, X_i are independent compositional variables used to describe

497   spinel composition (Si, Ti, Fe, Mg, Cr, Al, and Mn; Sack & Ghiorso, 1991b); they are listed

498   in Table A1. Other parameters (b, c_0–c_{14}) are regression coefficients fitted to the

499   experimental dataset through a polynomial curve-fitting approach. In Eq. 3, because the

500   term $X_{\mathrm{Mg}^{2+}}^{\mathrm{TET}} X_{\mathrm{Al}^{3+}}^{\mathrm{OCT}}$ is proportional to spinel Al$_2$O$_3$ content, we can simplify the equation by

501   replacing the $\ln\left(\frac{X_{\mathrm{Al}_2\mathrm{O}_3}^{\mathrm{Ol}}}{X_{\mathrm{Mg}^{2+}}^{\mathrm{TET}} X_{\mathrm{Al}^{3+}}^{\mathrm{OCT}}}\right)$ with $\ln K_{\mathrm{D}_{\mathrm{Al}}}$. The final regression on the training dataset is:

$$T\ (\mathrm{K}) = \frac{10{,}000 \times \varphi^{\mathrm{Spl}}}{-0.168 \times (\ln K_{\mathrm{D}_{\mathrm{Al}}} + 0.654)} \tag{5}$$

502   where

20

$$\varphi^{\mathrm{Spl}} = 1.487X_2 - 0.593X_2^2 - 0.630X_2^{\frac{1}{2}} \tag{6}$$

$$+ 0.390(1 - X_2)(1 + X_4 - X_2)$$

$$+ 0.009(1 - X_2)(X_3) - 2.492(1 - X_2)(X_4) + 0.065(1 - X_2)(X_5)$$

$$- 0.031X_3(X_3 + X_4 + X_5)$$

$$- 4.141X_4(X_3 + X_4 + X_5)$$

$$- 0.428X_5(X_3 + X_4 + X_5)$$

$$+ 4.637(X_3)(X_4) + 0.054(X_3)(X_5) + 10.803(X_4)(X_5) + 2.714$$

503 The regression result for Eq. 5 is shown in Fig. 5b and Table A2: the SEE and r^2 values for

504 the training dataset are ±20.2 °C and 0.97, respectively, RMSE on the test dataset is 29.0 °C,

505 and the p-value of the fit, where a no correlation alternative null hypothesis being tested

506 against, is 1.11e−16. The MCCV result shows that the median $\mathrm{SEE_{MCCV}}$ and r^2_{MCCV} values

507 for the training dataset are 20.2 °C and 0.97, respectively, and the median $\mathrm{RMSE_{MCCV}}$ value

508 for the test dataset is ~23.9 °C.

509

510 **Empirical expressions**

511 By using our expanded experimental dataset, we first recalibrated an empirical model

512 similar to the regression format of Coogan *et al.* (2014) but with unweighted multiple linear

513 regression (see supplementary material for a comparison with a weighted regression method,

514 Section 4):

$$T\ (\mathrm{K}) = \frac{10{,}000}{0.740(0.317) + 1.144(0.136)\mathrm{Cr\#} - 0.865(0.046)\ln K_{\mathrm{D\,Al}}} \tag{7}$$

515 The regression result of this new thermometer is shown in Fig. 5c and Table A2: the SEE

516 and r^2 values for the training dataset are ±44.8 °C and 0.83, respectively, RMSE on the test

517 dataset is 34.4 °C, and the p-value of the fit is 2.88e−36. The MCCV result shows that the

21

518   median SEE$_{MCCV}$ and r^2_{MCCV} values for the training dataset are 42.1 °C and 0.92,

519   respectively, and the median RMSE$_{MCCV}$ value for the test dataset is 43.3 °C.

520   Considering that Cr may have a coupled substitution with Al when entering olivine

521   to form a (MgAl)Cr$_2$O$_4$ structure (Hanson & Jones, 1998; Milman-Barris *et al*., 2008;

522   Jollands *et al*., 2018), we explored whether the Cr exchange between olivine and spinel

523   ($K_{D_{Cr}}$) would improve the empirical thermometric equation:

$$T\ (\text{K}) \tag{8}$$
$$= \frac{10,000}{0.049(0.241) - 0.657(0.040)\ln K_{D_{Al}} - 0.389(0.041)\ln K_{D_{Cr}} + 0.543(0.121)\text{Cr\#}}$$

524

525   Cr-free experiments were excluded during regression (Fig. 5d and Table A2). The SEE and

526   r^2 values for the training dataset are ±31.7 °C and 0.91, respectively, RMSE on the test

527   dataset is 39.1 °C, and the *p*-value of the fit is 3.79e−47. The MCCV result shows that the

528   SEE$_{MCCV}$ and r^2_{MCCV} values for the training dataset are 35.8 °C and 0.94, respectively, and

529   the median RMSE$_{MCCV}$ value for the test dataset is 34.2 °C. We are aware that Eq. 8 includes

530   all the regression variables from Eq. 7. To determine if the improved performance of Eq. 8

531   is due to more regression terms or statistical significance, we performed a *F*-test (see

532   Appendix B for further details on the *F*-test model). The results of the *F*-test show an *F*

533   score of 88.4 and a *p*-value of 5.4e−15, which is statistically significant ($p < 0.05$) at 95%

534   confidence. Therefore, the incorporation of Cr exchange as $K_{D_{Cr}}$ into Eq. 8 produced a

535   statistically superior fit compared to Eq. 7.

536

537   **Factors affecting the performance of the models**

538   *Dependence of the models on spinel composition and olivine–spinel Cr exchange*

539   Previous studies have noted limitations of the original thermometric calibration due

540   to the restricted range of Cr# values used in the calibration (e.g., Heinonen *et al*., 2015；Xu

541   & Liu, 2016; Trela *et al*., 2017). In Fig. 6, we compare spinel Cr# with the Δ*T* calculated

542   using our three new models and that of Coogan *et al*. (2014). There is no apparent

543   correlation between ΔT and spinel Cr# calculated using Eqs. 5, 7, and 8, whereas the model

544   of Coogan $et\ al.$ (2014) shows a moderate correlation ($r^2 = 0.41$). Spinel Fe^{3+}/Fe^{2+} has a

545   moderate impact on ΔT using the model of Coogan $et\ al.$ ($r^2 = 0.47$), a limited impact using

546   Eq. 7 ($r^2 = 0.24$), and negligible impacts on Eqs. 5 and 8 (Fig. S6). The effect of spinel TiO_2

547   content was negligible for all models (Fig. S7).

548   Spinel Mg# and $Fe^{3+}/(Fe^{3+} + Cr + Al)$ affect the performance of Eq. 7 ($r^2 = 0.28$ and

549   0.66, respectively) and the model of Coogan $et\ al.$ (2014; $r^2 = 0.13$ and 0.76, respectively),

550   but have less effect on Eqs. 5 and 8 (Figs. 7, 8). Similarly, $K_{D_{Cr}}$ has a moderate effect on Eq.

551   7 and the model of Coogan $et\ al.$ (2014), but not on Eqs. 5 and 8, suggesting that $K_{D_{Cr}}$ is

552   indeed an important parameter for improving the accuracy of the empirical models (Fig. S8).

553   The thermodynamic model Eq. 5 including the spinel composition, may also mimic the

554   effect of $K_{D_{Cr}}$. The correlation of ΔT with the spinel compositional parameters and $K_{D_{Cr}}$

555   indicates that using only spinel Cr# and $K_{D_{Al}}$ is not sufficient to accurately predict

556   temperature in all circumstances, particularly when spinel has a low Mg# or high $Fe^{3+}/(Fe^{3+}$

557     $+ Cr + Al)$ as is often observed in natural LIP spinels (Fig. 1). In such cases, the model of

558   Coogan $et\ al.$ (2014) and Eq. 7 may have larger uncertainties and may strongly overestimate

559   temperature.

560

561     $Dependence\ of\ the\ thermometers\ on\ fO_2,\ H_2O,\ and\ pressure$

562   fO_2 does not strongly affect the accuracy of the temperature calibrations of any of

563   the models, but a weak negative correlation was observed for Eq. 8 (Fig. S9). We further

564   tested the effect of melt water content and pressure with our reanalyzed experimental dataset

565   (three hydrous experiments with 3.7–7.4 wt.% H_2O in the experimental glass; seven dry

566   high-pressure experiments at 500–1350 MPa). Although water is known to have a profound

567   effect on the olivine liquidus (Médard & Grove, 2008), this appears to be of negligible

568   consequence on the accuracy of any of the thermometric models (Fig. S10). A potential

569   explanation of this is that the effect of water is compensated by changes to the olivine and

ORIGINAL UNEDITED MANUSCRIPT

570   spinel compositions. Pressure, however, shows a moderate correlation in all models,

571   although the results are within the uncertainty of each model (Fig. 9). It is unclear whether

572   this correlation is due to sample bias related to the sparse high pressure experiments, or if

573   pressure may affect on the molar volume of spinel and site occupancy (Hamecher *et al.*,

574   2013). Nonetheless, D'Souza *et al.* (2020) proposed that pressure has no effect on the model

575   of Coogan *et al.* (2014).

576

577   **DISCUSSION**

578   In this section, we discuss the limits of the thermometric models and their sensitivities to

579   subsolidus re-equilibration. We then establish a protocol for selecting the appropriate model

580   for applications to natural samples. Finally, we apply our models to constrain mantle

581   melting conditions and lithological components in a range of geological settings and use

582   thermodynamic calculations to assess potential re-equilibration in natural olivine-spinel

583   pairs.

584

585   **Concerns, limits, and sensitivities of the models**

586   Our thermodynamic model (Eq. 5) is accurate but involves the exchange of Fe and Mg,

587   which diffuse rapidly in spinel (Vogt *et al.*, 2015). This means that temperature estimates in

588   natural systems could be affected by low-temperature re-equilibration due to olivine-spinel

589   subsolidus Fe-Mg exchange during cooling. We note that the system itself doesn't have be

590   subsolidus, i.e., the olivine-spinel pair could crystallize at high temperature but experienced

591   a Fe-Mg reset after being carried along in an evolved melt, or set in a partially molten mush

592   before re-entrainment and eruption. The empirical model Eq. 8 does not involve Fe and Mg

593   but incorporates Cr exchange between olivine and spinel. Subsolidus Cr re-equilibration in

594   olivine, potentially caused by Cr reset between the carrier liquid, could also result in Eq. 8

595   potentially yielding anomalously low temperature estimates, we however note that the

596   diffusivity of Cr in olivine is poorly constrained and may vary with $f\mathrm{O}_2$ and Cr

597   concentrations in olivine (Ito & Ganguly 2006; Jollands *et al.*, 2018). In contrast, the

24

598   empirical models of Eq. 7 and Coogan *et al*. (2014) only involve slow diffusive elements in

599   spinel and olivine (Vogt *et al*., 2015; Spandler & O'Neill, 2010). Therefore they are not

600   impacted by low-temperature re-equilibration, but tend to overestimate temperature when

601   spinel has low Mg# or high $Fe^{3+}/(Fe^{3+} + Al^{3+} + Cr^{3+})$ (Figs. 7 and 8).

602   To quantitively investigate the sensitivities of Eq. 5 to Fe-Mg re-equilibration and

603   Eq. 8 to Cr re-equilibration in olivine, we performed two numerical simulations: 1) we

604   modeled Fe-Mg re-equilibration in a stoichiometric Cr-spinel with the formula (Mg,

605   Fe^{2+})(Al, Cr, Fe^{3+})$_2$O$_4$, and 2) we progressively added Cr_2O_3 to olivine to model Cr re-

606   equilibration. In the Fe-Mg re-equilibration model, Al diffusivity in olivine is slow

607   (Spandler & O'Neill, 2010), so we assumed that spinel exchanges only Fe^{2+} and Mg with

608   olivine and, therefore, the spinel Cr# remains constant at a fixed fO_2, which is consistent

609   with natural observations (Guo *et al*., 2009; Hu *et al*., 2022). Spinel Mg# were set to values

610   vary from 0.3 to 1 with an increment of 0.01 at each spinel Cr#, which we varied from 0.4 to

611   0.9 with the same increment to cover the whole range observed in nature. We held spinel

612   Fe^{3+}/Fe^{2+} constant at 0.5, corresponding to the median of natural spinel compositions,

613   Olivine Al_2O_3 content was set to 500 μg/g. Temperatures were then calculated using Eq. 5.

614   Because the mechanism of Cr re-equilibration in olivine has not been well determined

615   (Milman-Barris *et al*., 2008; Shea *et al.,* 2019; Lang *et al.,* 2022), we modeled two scenarios.

616   In the first scenario we assumed a decoupled substitution between Cr and Al, i.e., the Cr

617   content changes but the Al content remains constant, consistent with our experimental

618   observation. In the second scenario we assumed coupled substitution of Cr and Al with a

619   molar ratio of 1, similar to the observations of Milman-Barris *et al*. (2008) in a fast growth

620   regime. Both scenarios olivine Cr_2O_3 start from 200 to 1500 μg/g. Olivine Al_2O_3 content

621   was set to 500 μg/g in the first scenario and range from 134 to 1006 μg/g in the second

622   scenario, holding molar Cr/Al = 1. Temperatures were then calculated using Eq. 8.

623   Our model results are shown in Fig. 10. Decreasing spinel Mg# and decreasing

624   olivine Cr_2O_3 content (both decoupled and coupled substitutions) return lower temperatures

625   when using Eqs. 5 and 8, respectively. For a given degree of Fe-Mg or Cr re-equilibration,

25

626 the decrease in apparent temperature after a given degree of re-equilibration is greater for

627 spinel with higher Cr#, whereas Eq. 5 tends to underestimate temperature for spinel with

628 lower Mg#.

629

630 **Selecting the appropriate model for application to natural samples**

631 The reliability of the empirical model in Eq. 7 is limited to a specific range of spinel

632 compositions and has larger errors on the temperature estimation compared to the

633 thermodynamic model Eq. 5 and the empirical model Eq. 8. In contrast, Eqs. 5 and 8 are

634 more precise but may be affected by chemical re-equilibration, as discussed above. Given

635 the greater uncertainties in the empirical expressions (Eqs. 7 and 8), for a fully equilibrated,

636 primitive olivine-spinel pair, we expect them to return temperatures scattering above and

637 below that returned by the thermodynamic expression (Eq. 5). In turn, we expect Eq. 5 to

638 return lower temperatures than the Eqs. 7 and 8 if diffusive re-equilibration occurs.

639 Therefore, we consider that Eqs. 7 or 8 should be used when Eq. 5 has a more than 50%

640 chance of underestimating the true temperature (i.e., when the mean temperatures estimated

641 using Eq. 5 and either Eq. 7 or 8 differ sufficiently that a *p*-value test on the distributions

642 having the same mean returns $p < 0.5$). Model selection is then determined by the likelihood

643 that Eq. 5 yields an underestimation. If the temperature estimated using Eq. 5 is higher than

644 that estimated using Eq. 7 or 8, the result from the thermodynamic expression should be

645 chosen. If not, a statistical *Z*-test is introduced to decide whether to choose the

646 thermodynamic expression or empirical expression (e.g., Snedecor & Cochran, 1989):

$$Z = \frac{|T_i - T_j|}{\sqrt{\sigma_{X_i}^2 + \sigma_{X_j}^2}} \qquad (9)$$

647 where σ_{X_i} and σ_{X_j} are the RMSEs of the two models being compared (Eqs. 5 vs. Eq. 7

648 and/or Eq. 8) and T_i and T_j are the respective temperature estimates. If $Z > 1.35$, there is a 50%

649 chance that the two temperatures differ by a value larger than that attributed to their

650 combined uncertainties, and that Eqs. 7 or 8 return a higher temperature which is closer to

26

651   the true value. If both Eqs. 7 and 8 are compared with Eq. 5, the pair that yields with the

652   higher Z score should be chosen to obtain a larger probability that the temperature estimates

653   are different from each other. The Z value of 1.35 represents a width of 1.35 standard

654   deviations, which is required for 50% of normal distributions with standard deviations given

655   by each model to lie between the mean $-\frac{1}{2}\left|T_i - T_j\right|$ and the mean $+\frac{1}{2}\left|T_i - T_j\right|$ (i and j

656   represent each thermometric model); i.e., when $Z < 1.35$, 50% of the estimated temperatures

657   should be more similar if they are measuring the same temperature. A python script and an

658   Excel spreadsheet to perform all relevant calculations can be found at

659   https://github.com/eazzzon/olspthermo). Table 3 lists all scenarios for selecting the

660   appropriate model.

661   To illustrate the use of the protocol outlined above, we provide two geological

662   examples. In the first example, we take an ocean island basalt from Pico Island (Azores,

663   Portugal) containing a Fo_{83} olivine crystal, which has two spinel inclusions (van Gerve *et al*.,

664   2021). X-ray chemical maps show no Al, Cr, or P zoning in the olivine and stable Al

665   concentration profiles were acquired from the olivine till approaching the spinel-olivine

666   boundaries (see in the Supplementary material, Section 5). The spinel inclusions have Mg#

667   ≈ 0.51 and $Fe^{3+}/(Fe^{3+} + Cr + Al) \approx 0.17$. The temperatures calculated using Eqs. 5, 7, and 8

668   are 1091 ± 23 °C, 1171 ± 43 °C, and 1184 ± 34 °C, respectively, with errors propagated

669   from both analytical and thermometric uncertainties. Because the thermodynamic expression

670   returns a lower temperature than the empirical expressions, we applied the Z-test model. The

671   results show $Z = 1.62$ between Eqs. 5, and 7 and $Z = 0.76$ between Eqs. 5 and 8. Because of

672   the larger Z-score, the result from Eq. 7 is statistically more robust, which is consistent with

673   the temperature estimated from a melt inclusion within the same crystal using liquid

674   thermometry (~1194 ± 46 °C; van Gerve *et al*., 2021) and previous experimental studies

675   (e.g., Toplis & Carroll, 1995; Grove *et al*., 1992). According to these results, Eq. 5

676   significantly underestimates the temperature by ~80 °C.

677   For our second example, we take four published analyses of a MORB sample (A25-

678   D20-8) from Coogan *et al.* (2014), which contains an Fo_{91} olivine and a spinel with Mg# =

679   0.81. Eqs. 5, 7, and 8 return temperatures of 1265 ± 23 °C, 1235 ± 43 °C, and 1198 ± 34 °C,

680   respectively. Here, the thermodynamic expression is chosen because it returns a higher

681   temperature than the empirical expressions, hence the recommended temperature is 1265 ±

682   23 °C.

683

684   **Application of the extended OSAT to natural basalts**

685   Here, we apply our new thermometers to basalts from various settings: the Siqueiros MOR,

686   Iceland and Skye in the North Atlantic igneous province (NAIP), and the Emeishan,

687   Etendeka, and Caribbean LIPs. The results of different models are shown in Table 4 and Fig.

688   11. In each case, and for each analysis, we chose results according to the *Z*-test protocol

689   described above. For comparison, all temperature estimates from each model are shown in

690   Fig. S11. Given the similarity of spinel compositions from MORB, Iceland and Skye with

691   those from experiments used in the previous calibration of Coogan *et al.* (2014) and Wan *et*

692   *al.* (2008), the new temperature estimates from our models are comparable or fall within

693   mutual uncertainties. Intra-plate igneous provinces generally have higher $Fe^{3+}/(Fe^{3+} + Cr +$

694   Al) and lower Mg# (Fig. 1), therefore the model of Coogan *et al.* (2014) significantly

695   overestimate the temperature by 30–100 °C (median) and 60−120 °C at the maximum.

696

697   *MORB (Siqueiros)*

698   MORB lavas erupted at Siqueiros are generated by near-adiabatic upwelling of the ambient

699   upper mantle (e.g., Gregg *et al.,* 2009). Siqueiros spinel has Cr# = 0.24–0.44, and potentially

700   experienced less Fe-Mg subsolidus re-equilibration, with generally high Mg# values (0.70–

701   0.81) and $Fe^{3+}/(Fe^{3+} + Cr + Al)$ values (0.03–0.07). Olivine contains 335–827 μg/g Al_2O_3

702   and 508–2,750 μg/g Cr_2O_3. Coogan *et al*. (2014) and Matthews *et al*. (2021) calculated the

703   co-crystallization temperature of Siqueiros olivine and spinel to be 1230^{+59}_{-91} °C (expressed

28

704 as median$^{+[95^{th} \text{ percentile} - \text{median}]}_{-[\text{median} - 5^{th} \text{ percentile}]}$, being consistent with the description of distribution

705 used in Matthews et al. [2021]). Our new estimated temperatures are 1258^{+37}_{-76} °C. These

706 new estimates generally agree with the previous studies, which we attribute to the spinel

707 composition in Siqueiros lavas being comparable to those used in the calibration

708 experiments of Coogan *et al.* (2014) and Wan *et al.* (2008).

709

710 *NAIP (Iceland and Skye)*

711 Iceland and Skye are within the NAIP, which is accepted as having a mantle-plume origin.

712 Spinel in Iceland has Cr# 0.24–0.60, Mg# 0.54–0.79 and $Fe^{3+}/(Fe^{3+} + Cr + Al)$ 0–0.13.

713 Olivine ins Iceland contain Al_2O_3 396–1,020 µg/g and Cr_2O_3 345–2,686 µg/g. Spinel in

714 Skye is slightly more primitive, containing Cr# 0.41–0.56, Mg# 0.70–0.77 and $Fe^{3+}/(Fe^{3+} +$

715 $Cr + Al)$ 0.03–0.06. Olivine in Skye has more Al_2O_3 (794–1,519 µg/g) and less Cr_2O_3

716 (1,030–1,890 µg/g). Previous crystallization temperature estimates (Spice *et al.*, 2016;

717 Matthews *et al.*, 2016) using the model of Coogan *et al.* (2014) gave crystallization

718 temperatures of 1283^{+84}_{-66} °C for Iceland and 1409^{+60}_{-65} °C for Skye. Our new results are

719 1275^{+52}_{-100} °C for Iceland and 1388^{+41}_{-53} °C for Skye, which are similar on the median values

720 but ~ 40 °C lower for the high temperature populations (on the 95th)

721

722 *Emeishan large igneous province*

723 The ~260 Ma Emeishan LIP in southwest China is considered to be of mantle-plume origin

724 (Chung & Jahn, 1995; Xu *et al.*, 2001; Xiao *et al.*, 2004). Emeishan spinel compositions are

725 much more varied compared to MORB, with Cr# = 0.42–0.72, Mg# = 0.48–0.72, and

726 $Fe^{3+}/(Fe^{3+} + Cr + Al) = 0.04–0.15$. Olivine contains 340–990 µg/g Al_2O_3 and 165–1,420

727 µg/g Cr_2O_3. Previous temperature estimates give a crystallization temperature of

728 1271^{+108}_{-55} °C (Xu & Liu, 2016). Our new estimate is 1224^{+109}_{-54} °C, with both the median

729 and 95th value being ~ 47 °C cooler. Here, the compositional deviation of the natural olivine

29

730   and spinel from those used in the previous calibration results in the overestimated

731   crystallization temperatures.

732

733   *Etendeka large igneous province*

734   The Etendeka LIP is the southern part of Paraná-Etendeka LIP, mainly outcropping in

735   Namibia and southern Angola (Thompson *et al.,* 2001; Gibson, 2002). The high

736   crystallization temperatures and high ^{3}He/^{4}He values (>26 R_A, reported relative to that of the

737   present-day atmosphere) of the lavas suggest a mantle plume origin (Stroncik *et al*., 2017).

738   Etendeka spinel compositions are quite variable, with Cr# = 0.40–0.70, Mg# = 0.24–0.76,

739   and $Fe^{3+}/(Fe^{3+} + Al^{3+} + Cr^{3+})$ = 0.04–0.31. Olivine contains 300–1,200 µg/g Al_2O_3 and 200–

740   2,200 µg/g Cr_2O_3. Jennings *et al*. (2019) calculated the olivine crystallization temperature

741   using the model of Coogan *et al*. (2014) to be 1323^{+151}_{-101} °C. Our new results are

742   1307^{+110}_{-88} °C, which are similar at the median value but 57 °C lower for the high

743   temperature populations (on the 95th).

744

745   *Caribbean large igneous province (Tortugal suite)*

746   The Tortugal suite in Costa Rica is considered to be the product of the initial melting of the

747   Galapagos plume in the Caribbean large igneous province (Alvarado *et al*., 1997; Trela *et al*.,

748   2017). Particularly, the Tortugal suite hosts high-Fo olivine (up to Fo_{94}) with compositions

749   overlapping those of olivine in Archaean komatiites and containing 321–1,114 µg/g Al_2O_3

750   and 807–2,195 µg/g Cr_2O_3. Tortugal suite spinel span a wide range of compositions, with

751   Cr# = 0.66–0.85, Mg# = 0.33–0.72, and $Fe^{3+}/(Fe^{3+} + Cr + Al)$ = 0.0–0.14. Trela *et al*. (2017)

752   used the model of Coogan *et al*. (2014) to estimate the crystallization temperature to be

753   1492^{+89}_{-173} °C. Our new estimates, however, are much lower, at 1425^{+77}_{-149} °C, which are

754   67 °C lower on the median and 79 °C lower for the high temperature populations (on the

755   95th).

756

Implications for mantle melting, mantle lithologies, and subsolidus re-equilibration

757

758 Significant overestimation of temperature is often observed when the model of Coogan *et al.*

759 (2014) is applied to specific geological settings (e.g., intra-plate igneous provinces). This

760 model was however abundantly used to assess mantle melting conditions and lithologies in

761 those cases (e.g., Matthews *et al.,* 2016; 2021) which therefore necessitate a revision.

762 Olivine crystallization temperatures can be converted to mantle T_p when a correction for the

763 latent heat of melting is considered (Putirka *et al.,* 2007), which is directly related to the

764 total melt fraction. The total melt fraction can be constrained from melting of a

765 homogeneous (e.g., Putirka *et al.,* 2007) or a heterogenous mantle source (Matthews *et al.,*

766 2016; 2021), and through geophysical observations of magmatic productivity, i.e., crustal

767 thickness at spreading centers or magma flux at ocean islands (McKenzie & Bickle, 1988;

768 Shorttle *et al.,* 2014; Matthews *et al.,* 2016; 2021).

769 To be self-consistent with previous T_p and lithology estimates, we applied the protocol of

770 Matthews *et al.* (2016; 2021) to estimate the mantle melting conditions and mantle

771 lithologies for the localities investigated in this study. In this melting model, crustal

772 thickness at oceanic spreading centers and magma flux at ocean islands are used as

773 observable proxies for magma productivity. A multi-lithology mantle melting model during

774 adiabatic decompression following Phipps Morgan (2001) and Shorttle *et al*. (2014) is used

775 to calculate melting behavior. The source lithologies are assumed to be in thermal

776 equilibrium. A full description of the mathematical and computational formulation is

777 available in Phipps Morgan (2001) and Shorttle *et al*. (2014). An extra constraint was added

778 to prevent negatively buoyant solution in intra-plate magmatism, i.e., the multi-lithology

779 mantle should be buoyant with respect to the ambient mantle during the plume-driven

780 upwelling. We used the python interface forward model pyMelt (version 1.96; Matthews *et*

781 *al*., 2022) to calculate the melting behavior of mantle compositions comprising multiple

782 lithologies. The model considers three lithologies: lherzolite (*matthews.klb1* lithology class

783 in pyMelt) and silica-deficient pyroxenite (*matthews.kg1* lithology class) from Matthews *et*

784   *al*. (2021), and non-melting harzburgite (*shorttle.harzburgite* lithology class) from Shorttle

785   *et al*. (2014).

786   To convert an observation of primary crystallization temperatures (T_{cry}) to the value

787   of T_p, the fractions of mantle lithologies (ϕ_{Hz}, the harzburgite fraction; ϕ_{Px}, the pyroxenite

788   fraction; and ϕ_{Lz}, the peridotite/lherzolite fraction), we used an inversion model of

789   Matthews *et al*. (2021), a Bayesian Monte Carlo inference method (Feroz & Hobson, 2008;

790   Feroz *et al*., 2009, 2013; Buchner *et al*., 2014) to find the set of solutions which can

791   reproduce T_{cry} and mantle lithologies with applicable constraints (e.g., crustal thickness,

792   magma flux). The inversion model parameters (lithospheric thickness, crustal thickness, the

793   fraction of pyroxenite derived melt, magma flux) were kept identical to Table 1 in Matthews

794   *et al*. (2021), also given in supplementary dataset (Table S4), except for the T_{cry}, which we

795   adapted to our new estimates above. We note that these parameters may not be the most

796   appropriate for all our tested localities, but the focus here is on the influence of changing T_{cry}

797   on mantle T_p and lithology estimates. The inversion model requires the selection of an

798   appropriate olivine composition and crystallization temperature as the starting point of the

799   calculation. Matthews *et al*. (2021) assumed Fo_{91} olivine as the composition equilibrated

800   with primitive mantle-derived melts based on the most primitive olivine observed in nature.

801   However, both experimental and natural observations (e.g., the Tortugal suite) have shown

802   olivine of higher Fo ($>Fo_{94}$), indicating that the source diversity controls primary olivine

803   compositions atdifferent localities (see further discussion below). Here, we chose the

804   maximum of our calculated T_{cry} estimates (the corresponding olivine Fo are close to or

805   higher than 91) at each locality as the primary olivine temperature to simplify the constraints

806   on the equilibrated olivine composition.

807   Our inversion results for T_p and mantle lithological fractions are summarized in

808   Table 5 and shown in Fig. 12, details are given in the supplementary dataset. Because

809   different model parameters are used to constrain mantle T_p in different methods (e.g.,

810   Putirka, 2005; 2016), we only compare our new T_p values with those of Matthews *et al*.

811   (2021) in Fig. 13 to be self-consistent.

812   Our new estimated T_p and lithology fractions (ϕ_{Hz} and ϕ_{Px}) for MORB (1355^{+24}_{-19} °C,

813     $0.34^{+0.25}_{-0.30}$, and $0.02^{+0.02}_{-0.02}$, respectively), Iceland (1518^{+21}_{-17} °C, $0.23^{+0.18}_{-0.17}$, $0.08^{+0.04}_{-0.04}$), Skye

814   (1550^{+80}_{-82} °C, $0.51^{+0.32}_{-0.39}$, $0.12^{+0.16}_{-0.10}$), and Etendeka (1577^{+106}_{-98} °C, $0.53^{+0.31}_{-0.38}$, $0.11^{+0.19}_{-0.10}$) are

815   comparable to those of Matthews *et al*. (2021). However, due to previous overestimation of

816   crystallization temperatures for intra-plate LIPs, our newly estimated T_p and lithological

817   fractions differ significantly from Matthews *et al*. (2021). Our respective results for

818   Emeishan (1481^{+87}_{-78} °C, $0.53^{+0.29}_{-0.36}$, $0.10^{+0.14}_{-0.09}$) return a median T_p that is 74 °C cooler than

819   previous inversions (Table 4), and our results for the Tortugal suite (1648^{+193}_{-91} °C, $0.50^{+0.31}_{-0.38}$,

820     $0.15^{+0.29}_{-0.13}$) return a median T_p that is 165 °C cooler, which leads to a remarkable difference

821   in the estimated lithological fractions (Table 4).

822   To verify the reliability of the mantle melting and lithological estimates, we

823   performed forward thermodynamic modeling based on the estimated mantle T_p and

824   lithological fractions to calculate the equilibrated olivine composition in composition–

825   temperature space. We used the Matlab/Julia Mineral Assemblages Gibbs Energy

826   Minimization package (MAGEMin v1.3.0; Riel *et al*., 2022) to calculate the equilibrium

827   melt composition of a given mantle lithology under mantle melting conditions calculated

828   from inversion. For the modeling, we use the thermodynamic database of Holland *et al*.

829   (2018). The KLB-1 peridotite (Wasylenki *et al.,* 2003) and MIX1G pyroxenite (Hirschmann

830   *et al.,* 2003) were mixed with the median ratio of the estimated lithological fractions to

831   generate an equilibrated melt with the mantle source for each locality. The equilibrated melt

832   then crystallizes mineral phases within a given temperature interval at the base of the crust

833   (same as the inversion model, see Table S3 in the supplementary dataset and Table 1 in

834   Matthews *et al*. [2021]) at each locality. The model results are compared to our estimated

835   crystallization temperatures at each locality in Fig. 11. The equilibrated olivine usually

836   includes sub-populations containing higher-Fo (>Fo$_{91}$) than those in the erupted lavas, but

33

837   are generally consistent with the crystallization temperatures calculated using our extended

838   OSAT, whereas the results of Coogan *et al*. (2014) mostly overestimate the temperature.

839

840   **CONCLUSIONS**

841   We revised the formalism of the olivine-spinel aluminum exchange thermometer by

842   performing new experiments and reanalyzing published experiments to extend the

843   calibration P, T, fO$_2$, and H$_2$O conditions. Three models were regressed on the extended

844   dataset: a thermodynamic-based model (Eq. 5) and two empirical models (Eqs. 7 and 8).

845   The thermodynamic model of Eq. 5 shows the best performance with the lowest

846   uncertainties. The exchange of Al and Cr between olivine and spinel significantly effects the

847   results when using the empirical models, whereas fO$_2$, water, and pressure have little to

848   moderate effects on all models. The empirical models may only be accurate within a

849   restricted spinel composition, leading to temperature overestimations by ~30–100 °C in

850   some intra-plate LIPs, but only minor differences in Iceland and MOR. These improved T_{cry}

851   estimates translate to a significant difference in the mantle T_p and lithological fractions

852   calculated for the investigated intra-plate LIPs.

853

854   **APPENDIX A. THERMODYNAMIC MODEL OF OLIVINE–SPINEL AL**

855   **PARTITIONING**

856   Here, we develop our thermodynamic formalism to understand the Al exchange between

857   olivine and spinel. The most plausible solution mechanism for the incorporation of Al into

858   olivine and Cr-spinel is (Coogan *et al*., 2014):

$$(MgAl^{TET})Al^{OCT}O_4^{Spl} = (MgAl^{TET})Al^{OCT}O_4^{Ol} \qquad (A.1)$$

859   Thus, the equilibrium of the reaction is written as:

$$\mu_{\mathrm{MgAl_2O_4^{Ol}}} = \mu_{\mathrm{MgAl_2O_4^{Spl}}} \qquad (A.2)$$

860   where μ_{a^b} is the chemical potential of component a in phase b. For a given phase:

34

$$\mu_a = \mu_a^0 + RT\ln\alpha^a \qquad (A.3)$$

861 where μ_a^0 is the chemical potential of component a at standard state, α^a is the activity of

862 component a, R is the universal gas constant [8.314 J mol^{-1} K^{-1}], and T is the absolute

863 temperature in Kelvin.

864   For olivine, we can write:

$$\alpha_{MgAl_2O_4}^{Ol} = \gamma \times X_{MgAl_2O_4}^{Ol} \qquad (A.4)$$

$$X_{MgAl_2O_4}^{Ol} = (Al_2O_3^{Ol}{}_{wt.\%}/M_{Al_2O_3}) \times M_{MgAl_2O_4} \qquad (A.5)$$

865 where γ is the activity coefficient and M the molar weight of the component, and X is the

866 mole fraction. Combining Eqs. A.3–A.5, we obtain:

$$\mu_{MgAl_2O_4} = \mu_{MgAl_2O_4}^0 + RT\ln\left[\gamma \times \left(Al_2O_3^{Ol}{}_{wt.\%}/M_{Al_2O_3}\right) \times M_{MgAl_2O_4}\right] \qquad (A.6)$$

867 We apply a thermodynamic model involving cation site ordering (Sack, 1982; Sack &

868 Ghiorso, 1991a, 1991b) to describe the thermodynamic properties of the components in Cr-

869 spinel. In this model, spinel is assumed to be stoichiometrically perfect (R$_3$O$_4$), with *Fd3m*

870 space group symmetry. Five 'fictive' independent compositional variables (X_i) and ordering

871 parameters (s_i) are needed to describe the compositional change in Cr-spinel, which can be

872 calculated from mole fractions of cations in the spinel.

873   The independent compositional and ordering variables as well as the definitions of

874 site mole fractions are from Sack & Ghiorso (1991a, 1991b) and reported in Table. A1. The

875 molar Gibbs energy $\overline{G}$ is calculated from the vibrational Gibbs energy $\overline{G}^*$ and the ideal

876 molar configurational entropy $\overline{S}^{IC}$ as:

$$\overline{G} = \overline{G}^* - T\overline{S}^{IC} \qquad (A.7)$$

877 A second-degree Taylor expansion of the compositional and ordering variables is used to

878 describe the molar vibrational Gibbs energy as (Thompson Jr, 1969):

879

$$\overline{G}^* = g_0 + \sum_i \left(g_i X_i + g_{ii} X_i^2 + \sum_{j<i} g_{ij} X_i X_j \right)$$

$$+ \sum_i \sum_k \left(g_{ik} X_i s_k \right) \tag{A.8}$$

$$+ \sum_k \left(g_k s_k + g_{kk} s_k^2 + \sum_{l<k} g_{kl} s_k s_l \right)$$

880 where g terms are Taylor coefficients from Table 3 in Sack and Ghiorso (1991b). The

881 configurational entropy is calculated from compositional variables and site fractions as:

$$\overline{S}^{IC} = -R \sum_r \sum_c \bar{r} X_{c,r} \ln X_{c,r} \tag{A.9}$$

882 where $X_{c,r}$ is the fraction of cation c in site r in terms of X_i and s_i, and $\bar{r}$ is the number of r

883 sites per formula unit. A Darken equation is then used to manipulate and express the

884 chemical potential of the spinel endmembers (Darken & Gurry, 1953; Sack, 1982; Ghiorso,

885 1990; Sack & Ghiorso, 1991a):

$$\mu_j = \overline{G} + \sum_i n_{i,j} (1 - X_i) \left(\frac{\partial \overline{G}}{\partial X_i} \right)_{\frac{X_k}{X_l}, s_m} + \sum_i \left(q_{ij} - s_i \right) \left(\frac{\partial \overline{G}}{\partial s_i} \right)_{X_k, s_l} \tag{A.10}$$

886 where $n_{i,j}$ and $q_{i,j}$ represent coefficients of X_i and s_i, respectively, in 1 mol of spinel

887 component j. The chemical potential of component $MgAl_2O_4$ in a spinel solution can be

888 written as:

36

$$\mu_{\mathrm{MgAl_2O_4}}^{\mathrm{Spl}} = \overline{G}_2^* + RT\ln[(X_2)/(1+X_4)(1-X_3-X_4-X_5)^2]$$

$$+W_{Fe-Mg}^{TET}(1-X_2)(1+X_4-X_2)$$

$$+\Delta\overline{G}_{23}^0(1-X_2)(X_3)+\Delta\overline{G}_{24}^0(1-X_2)(X_4)+\Delta\overline{G}_{25}^0(1-X_2)(X_5)$$

$$+W_{1'3'}X_3(X_3+X_4+X_5)$$

$$+W_{1'4'}X_4(X_3+X_4+X_5)$$

(A.11)

$$+W_{1'5'}X_5(X_3+X_4+X_5)$$

$$-W_{3'4'}(X_3)(X_4)-W_{3'5'}(X_3)(X_5)$$

$$-W_{4'5'}(X_4)(X_5)$$

889   where $\overline{G}_2^*$ is the vibrational Gibbs energy of the $\mathrm{MgAl_2O_4}$ endmember. The Gibbs energy

890   along joins between vertices differing in composition (i.e., $\Delta\overline{G}_{23}^0$, $\Delta\overline{G}_{24}^0$, and $\Delta\overline{G}_{25}^0$) are

891   standard state Gibbs free energies of the Mg-Fe exchange reactions between aluminate (G_2),

892   chromate (G_3), titanate (G_4), and ferrite spinel (G_5). W_{Fe-Mg}^{TET}, W_{ij}, and $W_{ij'}$ are symmetric

893   regular solution parameters describing deviations of the Gibbs energy from ideal mixing. To

894   focus on Al partitioning between olivine and spinel, we combine Eqs. A.2, A.6, and A.10

895   with independent parameters X_i (Table A1) as:

37

$$\mu^0_{\mathrm{MgAl_2O_4^{Ol}}}+RT\ln\left[\gamma \times \left(Al_2O_3{^{Ol}_{wt.\%}}/M_{Al_2O_3}\right) \times M_{MgAl_2O_4}\right]$$

$$= \overline{G}^*_2+RT\ln[(X_2)/(1+X_4)(1-X_3-X_4-X_5)^2]$$

$$+W^{TET}_{Fe-Mg}(1 - X_2)(1 + X_4 - X_2)$$

$$+\Delta\overline{G}^0_{23}(1\text{-}X_2)(X_3)+\Delta\overline{G}^0_{24}(1\text{-}X_2)(X_4)+\Delta\overline{G}^0_{25}(1\text{-}X_2)(X_5)$$

$$+W_{1'3'}X_3(X_3+X_4+X_5)$$

$$+W_{1'4'}X_4(X_3+X_4+X_5)$$ (A.12)

$$+W_{1'5'}X_5(X_3+X_4+X_5)$$

$$-W_{3'4'}(X_3)(X_4)-W_{3'5'}(X_3)(X_5)$$

$$-W_{4'5'}(X_4)(X_5)$$

896 After re-organizing terms:

$$RT\ln[\gamma \times \mathrm{Al_2O_3}{^{Ol}_{wt.\%}}/((X_2)/(1+X_4)(1 - X_3 - X_4 - X_5)^2)]$$

$$= \overline{G}^*_2 \text{-} \mu^0_{\mathrm{MgAl_2O_4^{Ol}}}$$

$$+W_{TET}(1 - X_2)(1 + X_4 - X_2)$$

$$+\Delta\overline{G}^0_{23}(1\text{-}X_2)(X_3)+\Delta\overline{G}^0_{24}(1\text{-}X_2)(X_4)+\Delta\overline{G}^0_{25}(1\text{-}X_2)(X_5)$$

$$+W_{1'3'}X_3(X_3+X_4+X_5)$$ (A.13)

$$+W_{1'4'}X_4(X_3+X_4+X_5)$$

$$+W_{1'5'}X_5(X_3+X_4+X_5)$$

$$-W_{3'4'}(X_3)(X_4)-W_{3'5'}(X_3)(X_5)$$

$$-W_{4'5'}(X_4)(X_5)$$

38

897   On the left side of Eq. A.13, $(X_2)/(1+X_4)\left(1-X_3-X_4-X_5\right)^2$ is equal to $X_{Mg^{2+}}^{TET} X_{Al^{3+}}^{OCT^2}$; on the right

898   side of Eq. A.13, all parameters are constants or barely change with temperature (see Sack &

899   Ghiorso, 1991a), except $\mu_{MgAl_2O_4^{Ol}}^0$, $\overline{G}_2^*$ and the independent composition X_i. $\overline{G}_2^*$ can be

900   rewritten as $\left(c_1 X_2 + c_2 X_2^2 + c_3 X_2^{\frac{1}{2}}\right)$ following Eq. A.8, where c_1, c_2 and c_3 are constants

901   derived from the Taylor expansion coefficients. However, given that the standard state of

902    $MgAl_2O_4$ (i.e., $\mu_{MgAl_2O_4^{Ol}}^0$) in olivine is not well constrained, $\mu_{MgAl_2O_4^{Ol}}^0$, by definition, is

903   relevant to temperature at any given pressure and composition. We thus simplified

904    $\mu_{MgAl_2O_4^{Ol}}^0$ to be a function of temperature and independent of olivine composition given the

905   trace concentration of Al in olivine (Ganguly, 2008), and γ for Al_2O_3 in olivine can be

906   assumed to be 1. We thus encapsulate all parameters related to spinel as φ^{Spl}, and Eq. A.13

907   can be fitted with coefficients (c_i) replacing the regular solution parameters, and related to

908   the spinel composition as:

$$\ln\left(\frac{X_{Al_2O_3^{Ol}}}{X_{Mg^{2+}}^{TET} X_{Al^{3+}}^{OCT}}\right) + b = \frac{\varphi^{Spl}}{c_0 \times T} \tag{A.14}$$

909   where

$$\varphi^{Spl} = c_1 X_2 + c_2 X_2^2 + c_3 X_2^{\frac{1}{2}}$$

$$+ c_4(1 - X_2)(1 + X_4 - X_2)$$

$$+ c_5(1-X_2)(X_3) + c_6(1-X_2)(X_4) + c_7(1-X_2)(X_5)$$

$$+ c_8 X_3(X_3+X_4+X_5)$$

$$+ c_9 X_4(X_3+X_4+X_5)$$

$$+ c_{10} X_5(X_3+X_4+X_5)$$

$$- c_{11}(X_3)(X_4) - c_{12}(X_3)(X_5) - c_{13}(X_4)(X_5) + c_{14}$$

39

910   The coefficients b, and c_0–c_{12} can be then obtained by fitting the compositions of

911   experimental olivine and spinel pairs.

912

913   **APPENDIX B. *F*-TEST MODEL**

914   An *F*-test is a statistical test with the null hypothesis that a distribution follows an *F*-

915   distribution; *F*-tests have been used in solving geological problems involving regression

916   (e.g., Abouchami *et al*., 2005). An *F*-test is commonly used to compare two models that

917   give similar or identical results but use different numbers of parameters, with the aim of

918   determining which model is statistically better or whether the model with fewer parameters

919   is nested within the model with more parameters. In this case, the *F*-value can be calculated

920   as:

$$F = \frac{(RSS_1 - RSS_2)/(p_1 - p_2)}{RSS_2/(n - p_2)} \tag{B.1}$$

921   where RSS_i represents the residual sum of squares of model i; p_1 and p_2 represent the number

922   of parameters in models 1 (m_1) and 2 (m_2), and $p_1 < p_2$; and n is the amount of data points

923   used in the regressions. While comparing the two models, the null hypothesis is that m_2 is

924   not better than m_1 (i.e., that m_2 is an overfitting of m_1). When comparing the *F*-value with

925   the critical *F*-value, which can be calculated from the *F*-distribution with $(p_2 - p_1, n - p_2)$

926   degrees of freedom, if F exceeds the critical value, the associated *p*-value is small ($< 1 - \alpha$;

927   e.g., $\alpha = 0.05$ for 95% confidence) and then null hypothesis is rejected, meaning that m_2 is

928   indeed statistically better. If F is below the critical value, the associated *p*-value is larger

929   than α and m_1 is statistically better than m_2.

930 **REFERENCES**

931 Abouchami, W., Hofmann, A. W., Galer, S. J. G., Frey, F. A., Eisele, J. & Feigenson,
932 M. (2005). Lead isotopes reveal bilateral asymmetry and vertical continuity
933 in the Hawaiian mantle plume. *Nature* **434**, 851–856.

934 Alvarado, G. E., Denyer, P. & Sinton, C. W. (1997). The 89 Ma Tortugal komatiitic
935 suite, Costa Rica: implications for a common geological origin of the
936 Caribbean and Eastern Pacific region from a mantle plume. *Geology* **25**,
937 439–442.

938 Ariskin, A. A. & Nikolaev, G. S. (1996). An empirical model for the calculation of
939 spinel-melt equilibria in mafic igneous systems at atmospheric pressure: 1.
940 Chromian spinels. *Contributions to Mineralogy and Petrology* **123**, 282–292.

941 Ballhaus, C., Berry, R. F. & Green, D. H. (1991). High pressure experimental
942 calibration of the olivine-orthopyroxene-spinel oxygen geobarometer:
943 implications for the oxidation state of the upper mantle. *Contributions to*
944 *Mineralogy and Petrology*. **107**, 27–40.

945 Barr, J. A., Grove, T. L. & Wilson, A. H. (2009). Hydrous komatiites from
946 Commondale, South Africa: An experimental study. *Earth and Planetary*
947 *Science Letters* **284**, 199–207.

948 Batanova, V.G., Thompson, J.M., Danyushevsky, L.V., Portnyagin, M.V., Garbe-
949 Schönberg, D., Hauri, E., Kimura, J.I., Chang, Q., Senda, R., Goemann, K. &
950 Chauvel, C. (2019) New Olivine Reference Material for In Situ
951 Microanalysis. *Geostandards and Geoanalytical Research* **43**, 453–473.

952 Batanova, V. G., Sobolev, A. V. & Kuzmin, D. V. (2015). Trace element analysis of
953 olivine: High precision analytical method for JEOL JXA-8230 electron probe
954 microanalyser. *Chemical Geology* **419**, 149–157.

955 Beattie, P. (1993). Olivine-melt and orthopyroxene-melt equilibria. *Contributions to*
956 *Mineralogy and Petrology*. **115**, 103–111.

957 Bechon, T., Billon, M., Namur, O., Bolle, O., Fugmann, P., Foucart, H., Devidal, J.-
958 L., Delmelle, N. & Vander Auwera, J. (2022). Petrology of the magmatic
959 system beneath Osorno volcano (Central Southern Volcanic Zone, Chile).
960 *Lithos* **426–427**, 106777.

961 Blundy, J., Melekhova, E., Ziberna, L., Humphreys, M. C. S., Cerantola, V.,
962 Brooker, R. A., McCammon, C. A., Pichavant, M. & Ulmer, P. (2020).
963 Effect of redox on Fe–Mg–Mn exchange between olivine and melt and an
964 oxybarometer for basalts. *Contributions to Mineralogy and Petrology* **175**,
965 103.

966 Borisova, A. Y., Zagrtdenov, N. R., Toplis, M. J. & Guignard, J. (2020). New model
967 of chromite and magnesiochromite solubility in silicate melts. *arXiv preprint.*

968 Brown Krein, S., Molitor, Z. J. & Grove, T. L. (2021). ReversePetrogen: A
969 Multiphase Dry Reverse Fractional Crystallization-Mantle Melting

970   Thermobarometer Applied to 13,589 Mid-Ocean Ridge Basalt Glasses.
971   *Journal of Geophysical Research: Solid Earth* **126**, e2020JB021292.

972   Buchner, J. *et al.* (2014). X-ray spectral modelling of the AGN obscuring region in
973   the CDFS: Bayesian model selection and catalogue. *Astronomy &*
974   *Astrophysics* **564**, A125.

975   Campbell, I. H. & Griffiths, R. W. (1990). Implications of mantle plume structure
976   for the evolution of flood basalts. *Earth and Planetary Science Letters* **99**,
977   79–93.

978   Charlier, B., Grove, T. L., Namur, O. & Holtz, F. (2018). Crystallization of the lunar
979   magma ocean and the primordial mantle-crust differentiation of the Moon.
980   *Geochimica et Cosmochimica Acta* **234**, 50–69.

981   Chung, S.-L. & Jahn, B. (1995). Plume-lithosphere interaction in generation of the
982   Emeishan flood basalts at the Permian-Triassic boundary. *Geology* **23**, 889–
983   892.

984   Coogan, L. A., Saunders, A. D. & Wilson, R. N. (2014). Aluminum-in-olivine
985   thermometry of primitive basalts: Evidence of an anomalously hot mantle
986   source for large igneous provinces. *Chemical Geology* **368**, 1–10.

987   Darken, L. S. & Gurry, R. W. (1953). *Physical chemistry of metals*. McGraw-Hill.

988   Droop, G. T. R. (1987). A general equation for estimating Fe^{3+} concentrations in
989   ferromagnesian silicates and oxides from microprobe analyses, using
990   stoichiometric criteria. *Mineralogical Magazine* **51**, 431–435.

991   D'Souza, R. J., Canil, D. & Coogan, L. A. (2020). Geobarometry for spinel
992   peridotites using Ca and Al in olivine. *Contributions to Mineralogy and*
993   *Petrology* **175**, 5.

994   Evans, T. M., C. O'Neill, H. St. & Tuff, J. (2008). The influence of melt
995   composition on the partitioning of REEs, Y, Sc, Zr and Al between forsterite
996   and melt in the system CMAS. *Geochimica et Cosmochimica Acta* **72**, 5708–
997   5721.

998   Falloon, T. J., Danyushevsky, L. V., Ariskin, A., Green, D. H. & Ford, C. E. (2007).
999   The application of olivine geothermometry to infer crystallization
1000 temperatures of parental liquids: Implications for the temperature of MORB
1001 magmas. *Chemical Geology* **241**, 207–233.

1002 Feroz, F. & Hobson, M. P. (2008). Multimodal nested sampling: an efficient and
1003 robust alternative to Markov Chain Monte Carlo methods for astronomical
1004 data analyses. *Monthly Notices of the Royal Astronomical Society* **384**, 449–
1005 463.

1006 Feroz, F., Hobson, M. P. & Bridges, M. (2009). MultiNest: an efficient and robust
1007 Bayesian inference tool for cosmology and particle physics. *Monthly Notices*
1008 *of the Royal Astronomical Society* **398**, 1601–1614.

1009 Feroz, F., Hobson, M. P., Cameron, E. & Pettitt, A. N. (2013). Importance nested
1010   sampling and the MultiNest algorithm. *arXiv preprint arXiv:1306.2144*.

1011 Ganguly, J. (2008). *Thermodynamics in earth and planetary sciences*.

1012 Gavrilenko, M., Batanova, V. G., Llovet, X., Krasheninnikov, S., Koshlyakova, A.
1013   N. & Sobolev, A. V. (2023). Secondary fluorescence effect quantification of
1014   EPMA analyses of olivine grains embedded in basaltic glass. Chemical
1015   Geology. 121328.

1016 Gavrilenko, M., Herzberg, C., Vidito, C., Carr, M. J., Tenner, T. & Ozerov, A.
1017   (2016). A Calcium-in-Olivine Geohygrometer and its Application to
1018   Subduction Zone Magmatism. Journal of Petrology 57, 1811–1832.

1019 Gee, L. L. & Sack, R. O. (1988). Experimental Petrology of Melilite Nephelinites.
1020   *Journal of Petrology* **29**, 1233–1255.

1021

1022 Ghiorso, M. S. (1990). Application of the Darken equation to mineral solid solutions
1023   with variable degrees of order-disorder. *American Mineralogist* **75**, 539–543.

1024 Ghiorso, M. S., Hirschmann, M. M., Reiners, P. W. & Kress, V. C. (2002). The
1025   pMELTS: A revision of MELTS for improved calculation of phase relations
1026   and major element partitioning related to partial melting of the mantle to 3
1027   GPa. *Geochemistry, Geophysics, Geosystems* **3**, 1–35.

1028 Ghiorso, M. S. & Sack, R. O. (1995). Chemical mass transfer in magmatic processes
1029   IV. A revised and internally consistent thermodynamic model for the
1030   interpolation and extrapolation of liquid-solid equilibria in magmatic systems
1031   at elevated temperatures and pressures. *Contributions to Mineralogy and
1032   Petrology* **119**, 197–212.

1033 Gibson, S. A. (2002). Major element heterogeneity in Archean to Recent mantle
1034   plume starting-heads. *Earth and Planetary Science Letters* 195, 59–74.

1035 Goltz, A. E., Krawczynski, M. J., Gavrilenko, M., Gorbach, N. V. & Ruprecht, P.
1036   (2020). Evidence for superhydrous primitive arc magmas from mafic
1037   enclaves at Shiveluch volcano, Kamchatka. Contributions to Mineralogy and
1038   Petrology. 175, 1–26.

1039

1040 Green, D. H. & Falloon, T. J. (2005). Primary magmas at mid-ocean
1041   ridges,"hotspots," and other intraplate settings: Constraints on mantle
1042   potential temperature. In: Foulger, G.R., Natland, J.H., Presnall, D.C.,
1043   Anderson, D.L. (eds.), Plates, Plumes and Paradigms. Geological Society of
1044   America Special Paper 388, 217–247.

1045 Gregg, P. M., Behn, M. D., Lin, J. & Grove, T. L. (2009). Melt generation,
1046   crystallization, and extraction beneath segmented oceanic transform faults.
1047   Journal of Geophysical Research: Solid Earth. 114.

1048

1049 Grove, T. L., Kinzler, R. J. & Bryan, W. B. (1992). Fractionation of mid-ocean ridge
1050   basalt (MORB). *Mantle flow and melt generation at mid-ocean ridges*. **71**,
1051   281–310.

1052 Guo, S., Ye, K., Chen, Y. & Liu, J.-B. (2009). A normalization solution to mass
1053   transfer illustration of multiple progressively altered samples using the
1054   isocon diagram. *Economic Geology* **104**, 881–886.

1055 Hamecher, E. A., Antoshechkina, P. M., Ghiorso, M. S. & Asimow, P. D. (2013).
1056   The molar volume of FeO–MgO–Fe2O3–Cr2O3–Al2O3–TiO2 spinels.
1057   Contributions to Mineralogy and Petrology 165, 25–43

1058 Hanson, B. & Jones, J. H. (1998). The systematics of Cr3+ and Cr2+ partitioning
1059   between olivine and liquid in the presence of spinel. *American Mineralogist*
1060   **83**, 669–684.

1061 Heinonen, J. S., Jennings, E. S. & Riley, T. R. (2015). Crystallisation temperatures
1062   of the most Mg-rich magmas of the Karoo LIP on the basis of Al-in-olivine
1063   thermometry. *Chemical Geology* **411**, 26–35.

1064 Herzberg, C. & Asimow, P. D. (2015). PRIMELT3 MEGA.XLSM software for
1065   primary magma calculation: Peridotite primary magma MgO contents from
1066   the liquidus to the solidus. *Geochemistry, Geophysics, Geosystems* **16**, 563–
1067   578.

1068 Herzberg, C., Asimow, P. D., Arndt, N., Niu, Y., Lesher, C. M., Fitton, J. G.,
1069   Cheadle, M. J. & Saunders, A. D. (2007). Temperatures in ambient mantle
1070   and plumes: Constraints from basalts, picrites, and komatiites. *Geochemistry,*
1071   *Geophysics, Geosystems* **8**.

1072 Hirschmann, M. M., Kogiso, T., Baker, M. B. & Stolper, E. M. (2003). Alkalic
1073   magmas generated by partial melting of garnet pyroxenite. Geology 31, 481–
1074   484.

1075 Holland, T. J., Green, E. C. & Powell, R. (2018). Melting of peridotites through to
1076   granites: a simple thermodynamic model in the system KNCFMASHTOCr.
1077   Journal of Petrology 59, 881–900.

1078 Hu, W.-J., Zhou, M.-F., Yudovskaya, M. A., Vikentyev, I. V., Malpas, J. & Zhang,
1079   P.-F. (2022). Trace Elements in Chromite as Indicators of the Origin of the
1080   Giant Podiform Chromite Deposit at Kempirsai, Kazakhstan. *Economic*
1081   *Geology* **117**, 1629–1655.

1082 Ito, M. & Ganguly, J. (2006). Diffusion kinetics of Cr in olivine and 53Mn–53Cr
1083   thermochronology of early solar system objects. *Geochimica et*
1084   *Cosmochimica Acta* **70**, 799–809.

1085 Jennings, E., Buisman, I. & Coull, P. (2020). *Investigating mantle melting*
1086   *temperatures on Earth, Mars and the Moon using Al-in-olivine thermometry*.
1087   *AGU Fall Meeting Abstracts*.

44

1088 Jennings, E. S., Gibson, S. A. & Maclennan, J. (2019). Hot primary melts and
1089   mantle source for the Paraná-Etendeka flood basalt province: New
1090   constraints from Al-in-olivine thermometry. *Chemical Geology* **529**, 119287.

1091 Jochum, K.P., Stoll, B., Herwig, K., Willbold, M., Hofmann, A.W., Amini, M.,
1092   Aarburg, S., Abouchami, W., Hellebrand, E., Mocek, B. & Raczek, I. (2006).
1093   MPI-DING reference glasses for in situ microanalysis: New reference values
1094   for element concentrations and isotope ratios. *Geochemistry, Geophysics,*
1095   *Geosystems* **7**.

1096 Jollands, M. C., O'Neill, H. St. C., Van Orman, J., Berry, A. J., Hermann, J.,
1097   Newville, M. & Lanzirotti, A. (2018). Substitution and diffusion of Cr2+ and
1098   Cr3+ in synthetic forsterite and natural olivine at 1200–1500 °C and 1 bar.
1099   *Geochimica et Cosmochimica Acta* **220**, 407–428.

1100 Kamenetsky, V. S., Crawford, A. J. & Meffre, S. (2001). Factors controlling
1101   chemistry of magmatic spinel: an empirical study of associated olivine, Cr-
1102   spinel and melt inclusions from primitive rocks. Journal of Petrology 42,
1103   655–671.

1104 Katsura, T. & Ito, E. (1989). The system Mg2SiO4-Fe2SiO4 at high pressures and
1105   temperatures: Precise determination of stabilities of olivine, modified spinel,
1106   and spinel. *Journal of Geophysical Research: Solid Earth* **94**, 15663–15670.

1107 Koshlyakova, A. N., Sobolev, A. V., Krasheninnikov, S. P., Batanova, V. G. &
1108   Borisov, A. A. (2022). Ni partitioning between olivine and highly alkaline
1109   melts: An experimental study. Chemical Geology 587, 120615.

1110 Krasheninnikov, S. P., Sobolev, A. V., Batanova, V. G., Kargaltsev, A. A. &
1111   Borisov, A. A. (2017). Experimental testing of olivine–melt equilibrium
1112   models at high temperatures. Doklady Earth Sciences 919–922.

1113 Lang, S., Mollo, S., France, L., Misiti, V. & Nazzari, M. (2022). Partitioning of Ti,
1114   Al, P, and Cr between olivine and a tholeiitic basaltic melt: Insights on
1115   olivine zoning patterns and cation substitution reactions under variable
1116   cooling rate conditions. *Chemical Geology* 120870.

1117 Li, J., Huang, X.-L., Li, X.-H., Chu, F.-Y., Zhu, J.-H., Zhu, Z.-M. & Wang, H.
1118   (2021). Anomalously hot mantle source beneath the Dragon Flag
1119   Supersegment of the Southwest Indian Ridge: New evidence from
1120   crystallisation temperatures of mid-ocean ridge basalts. *Lithos* 106221.

1121 Llovet, X., Pinard, P. T., Donovan, J. J. & Salvat, F. (2012). Secondary fluorescence
1122   in electron probe microanalysis of material couples. *Journal of Physics D:*
1123   *Applied Physics* **45**, 225301.

1124 Llovet, X. & Salvat, F. (2017). PENEPMA: A Monte Carlo Program for the
1125   Simulation of X-Ray Emission in Electron Probe Microanalysis. Microscopy
1126   and Microanalysis 23, 634–646.

1127 Llovet, X., Gavrilenko, M., Batanova, V. G. & Sobolev, A. V. (2023). Element
1128   Depletion Due to Missing Boundary Fluorescence in Electron Probe

1129   Microanalysis: The Case of Ni in Olivine. *Microscopy and Microanalysis* **00**,
1130   1–15.

1131   Matthews, S., Shorttle, O. & Maclennan, J. (2016). The temperature of the Icelandic
1132   mantle from olivine-spinel aluminum exchange thermometry: Mantle
1133   temperature from geothermometry. *Geochemistry, Geophysics, Geosystems*
1134   **17**, 4725–4752.

1135   Matthews, S., Wong, K., Shorttle, O., Edmonds, M. & Maclennan, J. (2021). Do
1136   Olivine Crystallization Temperatures Faithfully Record Mantle Temperature
1137   Variability? *Geochemistry, Geophysics, Geosystems* **22**, e2020GC009157.

1138
1139   Matthews, S., Wong, K. & Gleeson, M. (2022). *PyMelt: An extensible Python*
1140   *engine for mantle melting calculations. Volcanica* 5(2), 469-475.Matthews,
1141   S., Wong, K., Shorttle, O., Edmonds, M. & Maclennan, J. (2021). Do Olivine
1142   Crystallization Temperatures Faithfully Record Mantle Temperature
1143   Variability? *Geochemistry, Geophysics, Geosystems* **22**, e2020GC009157.

1144   Matzen, A. K., Baker, M. B., Beckett, J. R. & Stolper, E. M. (2011). Fe–Mg
1145   partitioning between olivine and high-magnesian melts and the nature of
1146   Hawaiian parental liquids. *Journal of Petrology* **52**, 1243–1263.

1147   Matzen, A. K., Baker, M. B., Beckett, J. R. & Stolper, E. M. (2013). The
1148   temperature and pressure dependence of nickel partitioning between olivine
1149   and silicate melt. *Journal of Petrology* **54**, 2521–2545.

1150   Mckenzie, D. A. N. & Bickle, M. J. (1988). The volume and composition of melt
1151   generated by extension of the lithosphere. *Journal of petrology* **29**, 625–679.

1152   Médard, E. & Grove, T. L. (2008). The effect of H2O on the olivine liquidus of
1153   basaltic melts: experiments and thermodynamic models. *Contributions to*
1154   *Mineralogy and Petrology* **155**, 417–432.

1155   Milman-Barris, M. S., Beckett, J. R., Baker, M. B., Hofmann, A. E., Morgan, Z.,
1156   Crowley, M. R., Vielzeuf, D. & Stolper, E. (2008). Zoning of phosphorus in
1157   igneous olivine. *Contributions to Mineralogy and Petrology* **155**, 739–765.

1158   Mitchell, A. L. & Grove, T. L. (2015). Melting the hydrous, subarc mantle: the
1159   origin of primitive andesites. *Contributions to Mineralogy and Petrology* **170**,
1160   13.

1161   Molendijk, S. M., Namur, O., Kaeghetso, E. K., Mason, P.R.D, Smets, B., Vander
1162   Auwera, J.E. & Neave, D. A. (2023a). Petrology of the Nyiragongo volcano,
1163   DR Congo Goldschmidt 2023.

1164   Molendijk, S. M., Namur, O., Mason, P. R., Dubacq, B., Smets, B., Neave, D. A. &
1165   Charlier, B. (2023b). Trace element partitioning in silica-undersaturated
1166   alkaline magmatic systems. *Geochimica et Cosmochimica Acta* **346**, 29–53.

1167   Morgan, W. J. (1971). Convection plumes in the lower mantle. *Nature* **230**, 42–43.

1168 Neave, D. A. & Namur, O. (2022). Plagioclase archives of depleted melts in the
1169   oceanic crust. *Geology* **50**, 848–852.

1170 Neave, D. A., Namur, O., Shorttle, O. & Holtz, F. (2019). Magmatic evolution
1171   biases basaltic records of mantle chemistry towards melts from recycled
1172   sources. *Earth and Planetary Science Letters* **520**, 199–211.

1173 O'Hara, M. (1968). Are ocean floor basalts primary magma? *Nature* **220**, 683–686.

1174 Parman, S. W. & Grove, T. L. (2004). Harzburgite melting with and without H_2O:
1175   Experimental data and predictive modeling: Harzburgite melting. *Journal of*
1176   *Geophysical Research: Solid Earth* **109**.

1177 Phipps Morgan, J. (2001). Thermodynamics of pressure release melting of a veined
1178   plum pudding mantle. *Geochemistry, Geophysics, Geosystems* **2**.

1179 Poustovetov, A. & Roeder, P. (2001). Numerical modeling of major element
1180   distribution between chromian spinel and basaltic melt, with application to
1181   chromian spinel in MORBs. *Contributions to Mineralogy and Petrology* **142**,
1182   58–71.

1183 Prissel, T. C., Gross, J. & Draper, D. S. (2017). Application of Olivine-Spinel
1184   Eqilibria to Extraterrestrial Igneous Systems. *Lunar and Planetary Sciences*
1185   *Conference*.

1186 Putirka, K. (2016). Rates and styles of planetary cooling on Earth, Moon, Mars, and
1187   Vesta, using new models for oxygen fugacity, ferric-ferrous ratios, olivine-
1188   liquid Fe-Mg exchange, and mantle potential temperature. American
1189   Mineralogist 101, 819–840.

1190 Putirka, K. D. (2005). Mantle potential temperatures at Hawaii, Iceland, and the
1191   mid-ocean ridge system, as inferred from olivine phenocrysts: Evidence for
1192   thermally driven mantle plumes. *Geochemistry, Geophysics, Geosystems* **6**.

1193 Putirka, K. D. (2008). Thermometers and Barometers for Volcanic Systems. *Reviews*
1194   *in Mineralogy and Geochemistry* **69**, 61–120.

1195 Putirka, K. D., Perfit, M., Ryerson, F. J. & Jackson, M. G. (2007). Ambient and
1196   excess mantle temperatures, olivine thermometry, and active vs. passive
1197   upwelling. *Chemical Geology* **241**, 177–206.

1198 Ramsey, S. R., Howarth, G. H., Udry, A. & Gross, J. (2021). Nickel–manganese
1199   variability in olivine and Al-in-olivine thermometry for olivine-phyric
1200   shergottites. *Meteoritics & Planetary Science* 56(8), 1597–1618..

1201 Riel, N., Kaus, B. J. P., Green, E. C. R. & Berlie, N. (2022). MAGEMin, an
1202   Efficient Gibbs Energy Minimizer: Application to Igneous Systems.
1203   *Geochemistry, Geophysics, Geosystems* **23**, e2022GC010427.

1204 Roeder, P. L. & Emslie, R. F. (1970). Olivine-liquid equilibrium. *Contributions to*
1205   *mineralogy and petrology* **29**, 275–289.

47

1206 Sack, R. O. (1982). Spinels as petrogenetic indicators: Activity-composition
1207   relations at low pressures. *Contributions to Mineralogy and Petrology* **79**,
1208   169–186.

1209 Sack, R. O. & Ghiorso, M. S. (1991a). An internally consistent model for the
1210   thermodynamic properties of Fe−Mg-titanomagnetite-aluminate spinels.
1211   *Contributions to Mineralogy and Petrology* **106**, 474–505.

1212 Sack, R. O. & Ghiorso, M. S. (1991b). Chromian spinels as petrogenetic indicators:
1213   thermodynamics and petrological applications. *American Mineralogist* **76**,
1214   827–847.

1215 Shea, T., Hammer, J. E., Hellebrand, E., Mourey, A. J., Costa, F., First, E. C., Lynn,
1216   K. J. & Melnik, O. (2019). Phosphorus and aluminum zoning in olivine:
1217   contrasting behavior of two nominally incompatible trace elements.
1218   *Contributions to Mineralogy and Petrology* **174**, 85.

1219 Shorttle, O., Maclennan, J. & Lambart, S. (2014). Quantifying lithological
1220   variability in the mantle. *Earth and Planetary Science Letters* **395**, 24–40.

1221 Sleep, N. H. (1992). Time dependence of mantle plumes: Some simple theory.
1222   *Journal of Geophysical Research: Solid Earth* **97**, 20007–20019.

1223 Sleep, N. H. (1996). Lateral flow of hot plume material ponded at sublithospheric
1224   depths. *Journal of Geophysical Research: Solid Earth* **101**, 28065–28083.

1225 Snedecor, G. W. & Cochran, W. G. (1989). Statistical methods, 8thEdn. *Ames: Iowa
1226   State Univ. Press Iowa* **54**, 71–82.

1227 Sobolev, A. V., Asafov, E. V., Gurenko, A. A., Arndt, N. T., Batanova, V. G.,
1228   Portnyagin, M. V., Garbe-Schönberg, D. & Krasheninnikov, S. P. (2016).
1229   Komatiites reveal a hydrous Archaean deep-mantle reservoir. *Nature* **531**,
1230   628–632.

1231 Sossi, P. A., Klemme, S., O'Neill, H. St. C., Berndt, J. & Moynier, F. (2019).
1232   Evaporation of moderately volatile elements from silicate melts: experiments
1233   and theory. *Geochimica et Cosmochimica Acta* **260**, 204–231.

1234 Spandler, C. & O'Neill, H. St. C. (2010). Diffusion and partition coefficients of
1235   minor and trace elements in San Carlos olivine at 1,300°C with some
1236   geochemical implications. *Contributions to Mineralogy and Petrology* **159**,
1237   791–818.

1238 Spice, H. E., Fitton, J. G. & Kirstein, L. A. (2016). Temperature fluctuation of the
1239   Iceland mantle plume through time: Iceland mantle plume *t* fluctuations.
1240   *Geochemistry, Geophysics, Geosystems* **17**, 243–254.

1241 Stroncik, N. A., Trumbull, R. B., Krienitz, M.-S., Niedermann, S., Romer, R. L.,
1242   Harris, C. & Day, J. (2017). Helium isotope evidence for a deep-seated
1243   mantle plume involved in South Atlantic breakup. Geology 45, 827–830.

1244 Thompson Jr, J. B. (1969). Chemical reactions in crystals. *American Mineralogist:*
1245   *Journal of Earth and Planetary Materials* **54**, 341–375.

1246 Thompson, R. N., Gibson, S. A., Dickin, A. P. & Smith, P. M. (2001). Early
1247   Cretaceous basalt and picrite dykes of the southern Etendeka region, NW
1248   Namibia: windows into the role of the Tristan mantle plume in Paraná–
1249   Etendeka magmatism. *Journal of Petrology* 2049–2081.

1250 Thy, P. (1995). Low-pressure experimental constraints on the evolution of
1251   komatiites. *Journal of Petrology* **36**, 1529–1548.

1252 Toplis, M. J. (2005). The thermodynamics of iron and magnesium partitioning
1253   between olivine and liquid: criteria for assessing and predicting equilibrium
1254   in natural and experimental systems. *Contributions to Mineralogy and*
1255   *Petrology* **149**, 22–39.

1256 Toplis, M. J. & Carroll, M. R. (1995). An Experimental Study of the Influence of
1257   Oxygen Fugacity on Fe-Ti Oxide Stability, Phase Relations, and Mineral--
1258   Melt Equilibria in Ferro-Basaltic Systems. *Journal of Petrology* **36**, 1137–
1259   1170.

1260 Trela, J., Gazel, E., Sobolev, A. V., Moore, L., Bizimis, M., Jicha, B. & Batanova, V.
1261   G. (2017). The hottest lavas of the Phanerozoic and the survival of deep
1262   Archaean reservoirs. *Nature Geoscience* **10**, 451–456.

1263 Tuff, J., Takahashi, E. & Gibson, S. A. (2005). Experimental Constraints on the Role
1264   of Garnet Pyroxenite in the Genesis of High-Fe Mantle Plume Derived Melts.
1265   *Journal of Petrology* **46**, 2023–2058.

1266 van Gerve, T., Namur, O., Wieser, P., Lamadrid, H., Hulsbosch, N. & Neave, D.
1267   (2021). Constraints on Deep Magmatic Volatile Budgets from Olivine
1268   Hosted Melt Inclusions: Integrating 3D Imaging with Chemical
1269   Microanalysis. *AGU Fall Meeting Abstracts*, V41C-03.

1270 Vogt, K., Dohmen, R. & Chakraborty, S. (2015). Fe-Mg diffusion in spinel: New
1271   experimental data and a point defect model. *American Mineralogist* **100**,
1272   2112–2122.

1273 Wan, Z., Coogan, L. A. & Canil, D. (2008). Experimental calibration of aluminum
1274   partitioning between olivine and spinel as a geothermometer. *American*
1275   Mineralogist 93, 1142–1147.

1276 Wasylenki, L. E., Baker, M. B., Kent, A. J. & Stolper, E. M. (2003). Near-solidus
1277   melting of the shallow upper mantle: partial melting experiments on depleted
1278   peridotite. Journal of Petrology 44, 1163–1191.

1279 White, R. & McKenzie, D. (1989). Magmatism at rift zones: the generation of
1280   volcanic continental margins and flood basalts. *Journal of Geophysical*
1281   *Research: Solid Earth* **94**, 7685–7729.

1282 White, R. S. & McKenzie, D. (1995). Mantle plumes and flood basalts. *Journal of*
1283   *Geophysical Research: Solid Earth* **100**, 17543–17585.

1284 Wu, Y.-D., Yan, J.-H., Stagno, V., Nekrylov, N., Wang, J.-T. & Wang, H. (2022).
1285   Redox heterogeneity of picritic lavas with respect to their mantle sources in
1286   the Emeishan large igneous province. *Geochimica et Cosmochimica Acta*
1287   S0016703722000102.

1288 Xiao, L., Xu, Y. G., Mei, H. J., Zheng, Y. F., He, B. & Pirajno, F. (2004). Distinct
1289   mantle sources of low-Ti and high-Ti basalts from the western Emeishan
1290   large igneous province, SW China: implications for plume–lithosphere
1291   interaction. *Earth and Planetary Science Letters* **228**, 525–546.

1292 Xu, Q.-S. & Liang, Y.-Z. (2001). Monte Carlo cross validation. Chemometrics and
1293   Intelligent Laboratory Systems 56, 1–11.

1294 Xu, R. & Liu, Y. (2016). Al-in-olivine thermometry evidence for the mantle plume
1295   origin of the Emeishan large igneous province. *Lithos* **266–267**, 362–366.

1296 Xu, Y., Chung, S.-L., Jahn, B. & Wu, G. (2001). Petrologic and geochemical
1297   constraints on the petrogenesis of Permian–Triassic Emeishan flood basalts
1298   in southwestern China. *Lithos* **58**, 145–168.

1299 Zhang, L., Ren, Z.-Y., Zhang, L., Wu, Y.-D., Qian, S.-P., Xia, X.-P. & Xu, Y.-G.
1300   (2021). Nature of the Mantle Plume Under the Emeishan Large Igneous
1301   Province: Constraints From Olivine-Hosted Melt Inclusions of the Lijiang
1302   Picrites. *Journal of Geophysical Research: Solid Earth* **126**, e2020JB021022.

1303 Zhang, Y., Namur, O. & Charlier, B. (2023). Experimental study of high-Ti and
1304   low-Ti basalts: liquid lines of descent and silicate liquid immiscibility in
1305   large igneous provinces. *Contributions to Mineralogy and Petrology* **178**, 7.

1306

1307
1308

1309 **Figure captions**
1310
1311 **Fig. 1.** Spinel compositions in calibration experiments and natural rocks. (**a**) Ternary
1312 projection of spinel prism, Al-Cr-Fe^{3+}. (**b**) Spinel Cr# as a function spinel Mg# (**c**) Spinel
1313 TiO_2 (wt. %) as a function of spinel $Fe^{3+}/(Fe^{3+} + Cr + Al)$. (**d**) Spinel $Fe^{3+}/(Fe^{3+} + Cr + Al)$
1314 as a function of spinel $Fe^{2+}/(Fe^{2+}+Mg)$. Data from Barr et al. (2009), Mitchell and Grove
1315 (2015), Charlier et al. (2018), Parman and Grove (2004), and Thy (1995) are remeasured
1316 published experiments. Data from Matzen et al. (2011) and Hanson & Jones (1998) are used
1317 as part of the test dataset. See text for details on the calibration and test dataset. Natural
1318 samples are compiled from published studies: MORB (Coogan et al., 2014; Matthews et al.,
1319 2021;), Iceland (Spice et al., 2016; Matthews et al., 2016), Skye (Spice et al., 2016),
1320 Emeishan (Xu & Liu, 2016; Zhang et al., 2021; Li et al., 2021; Wu et al., 2022), Etendeka
1321 (Jennings et al., 2019), Tortugal (Trela et al., 2017). † represents experiments used in the
1322 training dataset, * represents experiments used in the test dataset. Error bar represents 1σ
1323 standard deviation and is not observable if it is smaller than the symbol.

1324 **Fig. 2. (a)** Al_2O_3 and **(b)** Cr_2O_3 concentrations in olivine (μg/g) as a function of Fo content
1325 (mol.%). Data sources are as in Fig. 1. Error bar represents 1σ standard deviation and is not
1326 observable if it is smaller than the symbol.
1327
1328 **Fig. 3.** Representative backscattered electron images of experimental products. Quench
1329 texture is observed in high temperature experiments (>1500 °C), euhedral olivine and spinel
1330 indicate the attainment of equilibrium in the experiments. Abbreviations: Gl, glass; Cr-Spl,
1331 Cr-spinel; Ol, olivine.
1332
1333 **Fig. 4.** Melt compositional variations as functions of melt MgO content (wt.%).
1334 Experimental data sources are as in Fig. 1. Error bar represents 1σ standard deviation and is
1335 not observable if it is smaller than the symbol.
1336
1337
1338 **Fig. 5.** Comparison of crystallization temperatures calculated using **(a)** the model of Coogan
1339 *et al.* (2014) and **(b–d)** Eqs. 5, 7, and 8, respectively. The green line represents the results of
1340 a Monte Carlo simulation showing the robustness of the fit when 1σ standard errors on
1341 spinel and olivine compositions are considered. The r^2 values represent the robustness of the
1342 linear regressions between the measured temperatures and predicted temperatures. The
1343 brown and purple fields represent temperatures within ±50 °C and ±100 °C. Data sources as
1344 in Fig. 1.
1345
1346 **Fig. 6.** Effects of spinel Cr# on **(a)** the OSAT of Coogan *et al.* (2014) and **(b–d)** the
1347 extended OSAT using Eqs. 5, 7, and 8, respectively. Data sources as in Fig. 1.
1348
1349 **Fig. 7.** Effects of spinel Mg# on **(a)** the OSAT of Coogan *et al.* (2014) and **(b–d)** the
1350 extended OSAT using Eqs. 5, 7, and 8, respectively. Data sources as in Fig. 1.
1351
1352 **Fig. 8.** Effects of spinel $Fe^{3+}/(Fe^{3+} + Cr + Al)$ on **(a)** the OSAT of Coogan *et al.* (2014) and
1353 **(b–d)** the extended OSAT using Eqs. 5, 7, and 8, respectively. Data sources as in Fig. 1.
1354
1355 **Fig. 9.** Effects of pressure (MPa) on **(a)** the OSAT of Coogan *et al.* (2014) and **(b–d)** the
1356 extended OSAT using Eqs. 5, 7, and 8, respectively. Data sources as in Fig. 1.
1357
1358 **Fig. 10.** Modeled effects of **(a)** Fe-Mg re-equilibration in spinel on temperatures estimated
1359 using Eq. 5 and **(b)** Cr re-equilibration (decoupled substitution) in olivine on temperatures
1360 estimated using Eq 8. **(c)** Cr re-equilibration (coupled substitution with Al) in olivine on
1361 temperatures estimated using Eq 8.
1362

51

Fig. 11. Estimated crystallization temperatures for natural samples. Gray symbols are results using the model of Coogan *et al*. (2014). Blue symbols are results using the extended OSAT of this study that passed the *Z*-test protocol described in the text. Red lines are the calculated equilibrated olivine compositions and temperatures from our forward thermodynamic modeling using MAGEMin. See text for more details. The histograms along the left axis show compare the distribution of results using our model to those using the model of Coogan *et al*. (2014). The histogram along the bottom axis shows the distribution of olivine Fo contents, which is the same in both datasets.

Fig. 12. Mantle lithologies and melting temperatures determined by our inversion analysis of natural samples using our extended OSAT, the contour lines represent density plot of the results.

Fig. 13. Comparison of estimated mantle potential temperatures in this study (colored) with those of Matthews *et al*. (2021; gray). The temperature excess on the right axis is calculated here relative to the median T_p of MORB (Siqueiros). The heights of the boxes show the interquartile range (25th–75th), and the upper and lower whisker bars show maximum and minimum values beyond which, data points represent outliers.
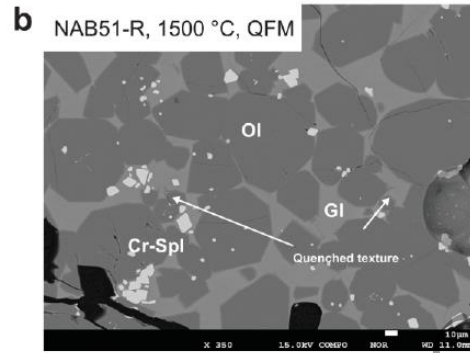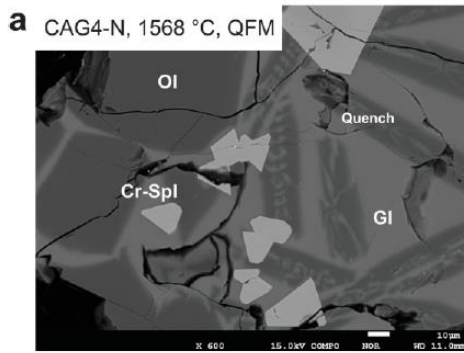
f1
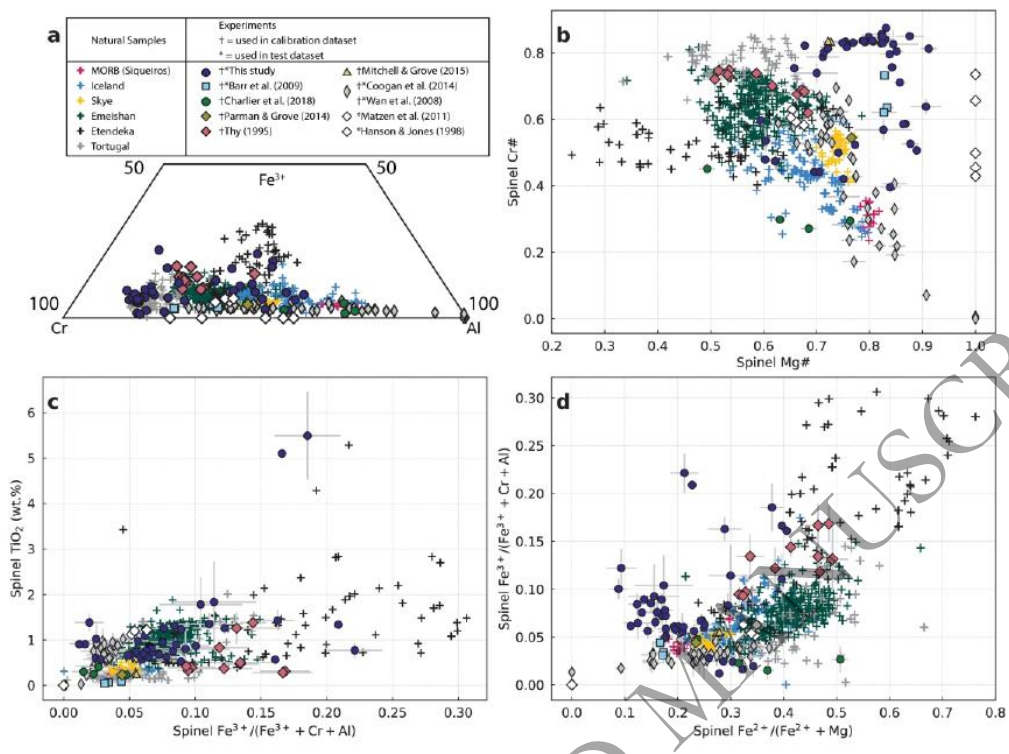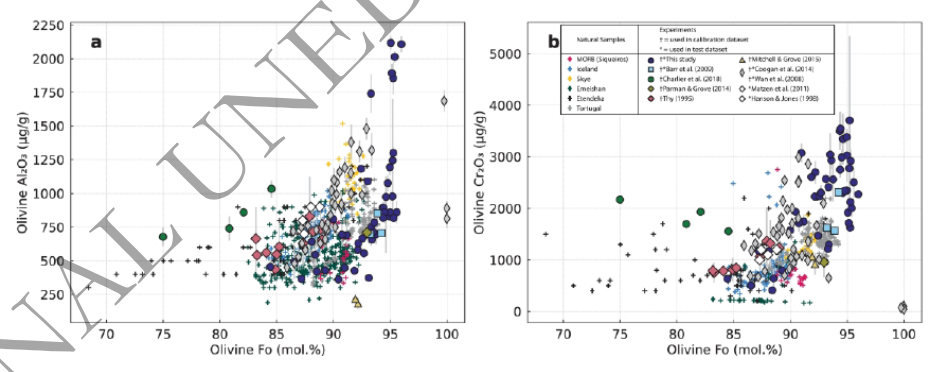
1418
1419
1420
1421
1422

f2

1423
1424
1425
1426
1427
1428
1429
1430
1431
1432
1433
1434
1435

a CAG4-N, 1568 °C, QFM
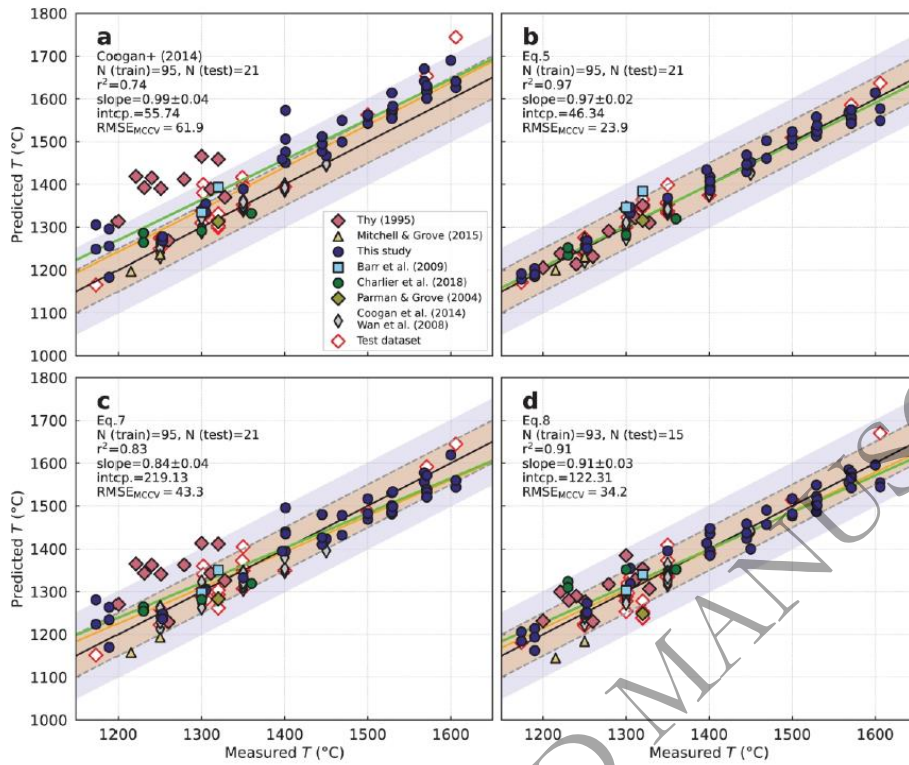
b NAB51-R, 1500 °C, QFM
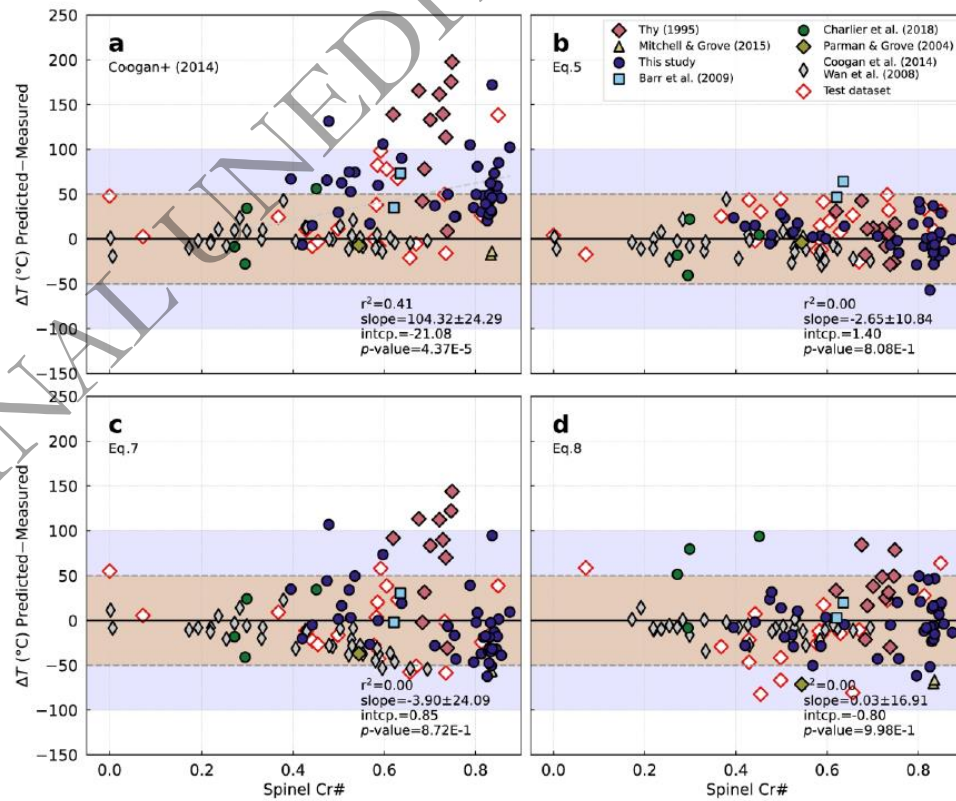
f3

1436
1437
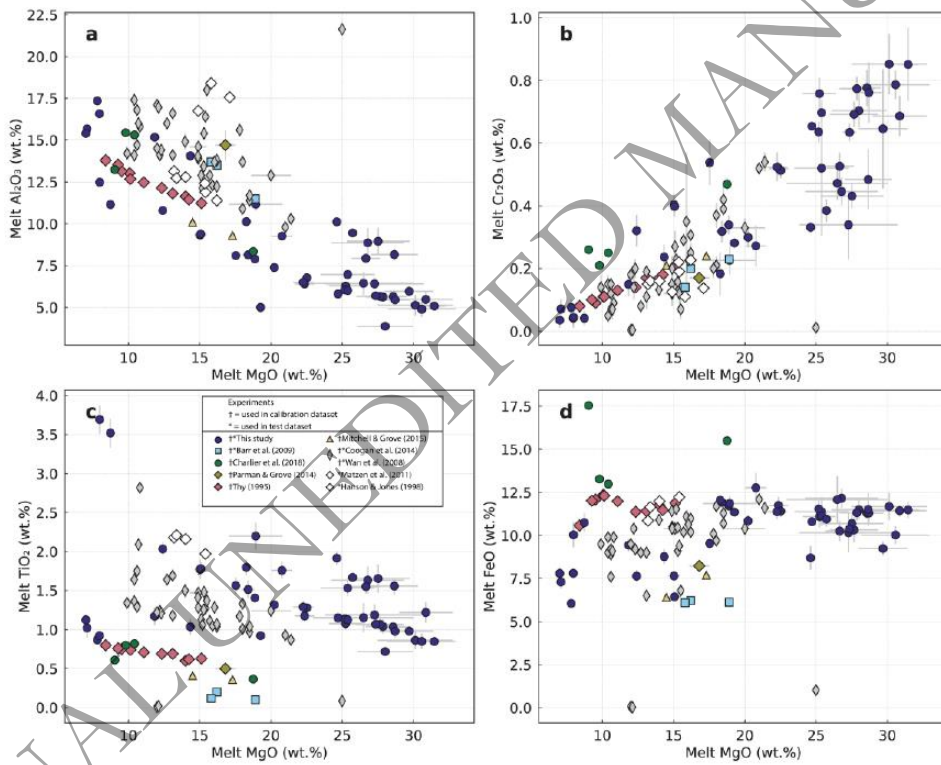
f4

1438
1439
1440
1441
1442
1443
1444
1445
1446
1447
1448
1449
1450
1451

f5

1452
1453
1454

f6

1455
1456
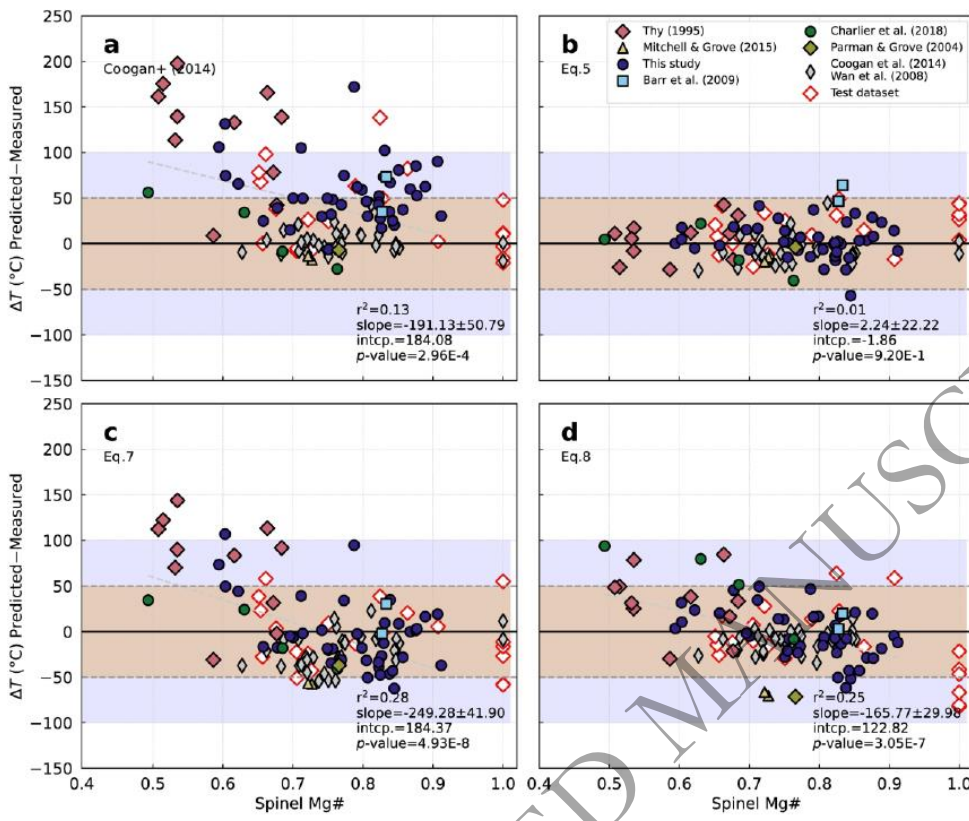
1457

1458
1459
1460

1461
1462
1463
1464
1465
1466
1467

f9
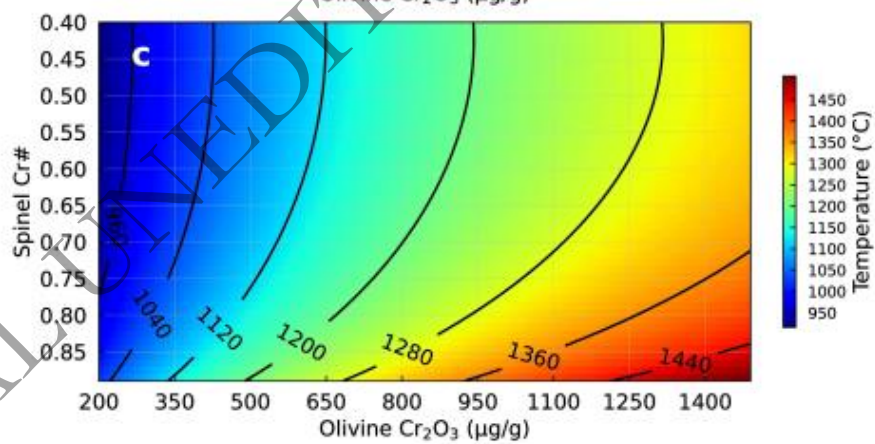
f10

1468
1469
1470
1471
1472
1473
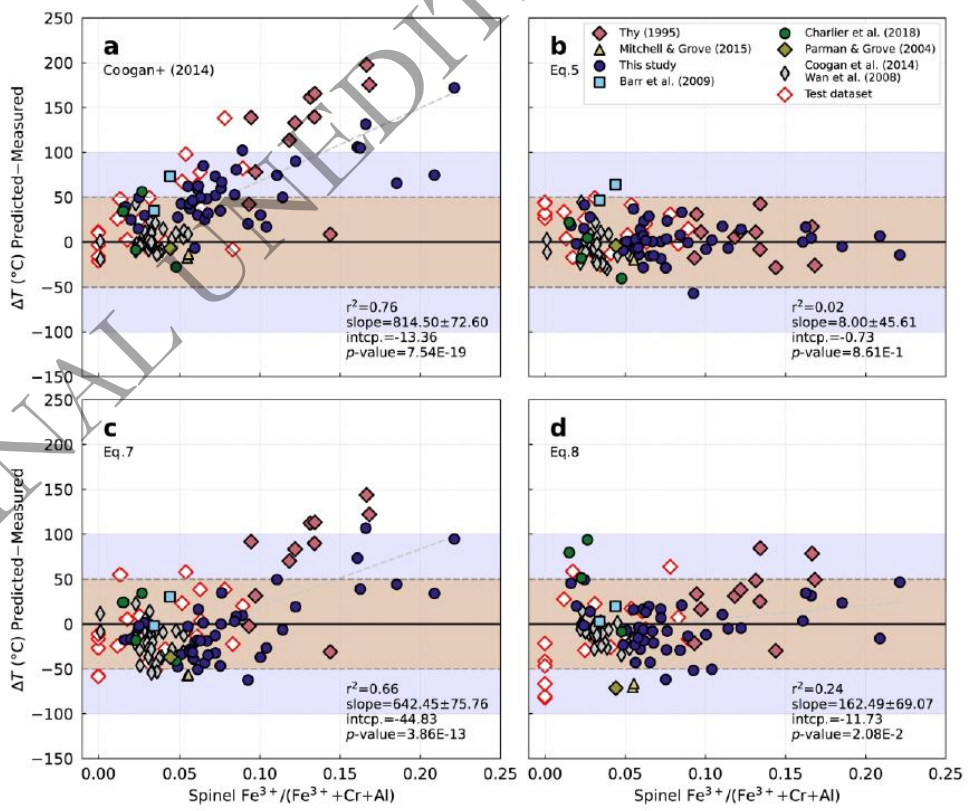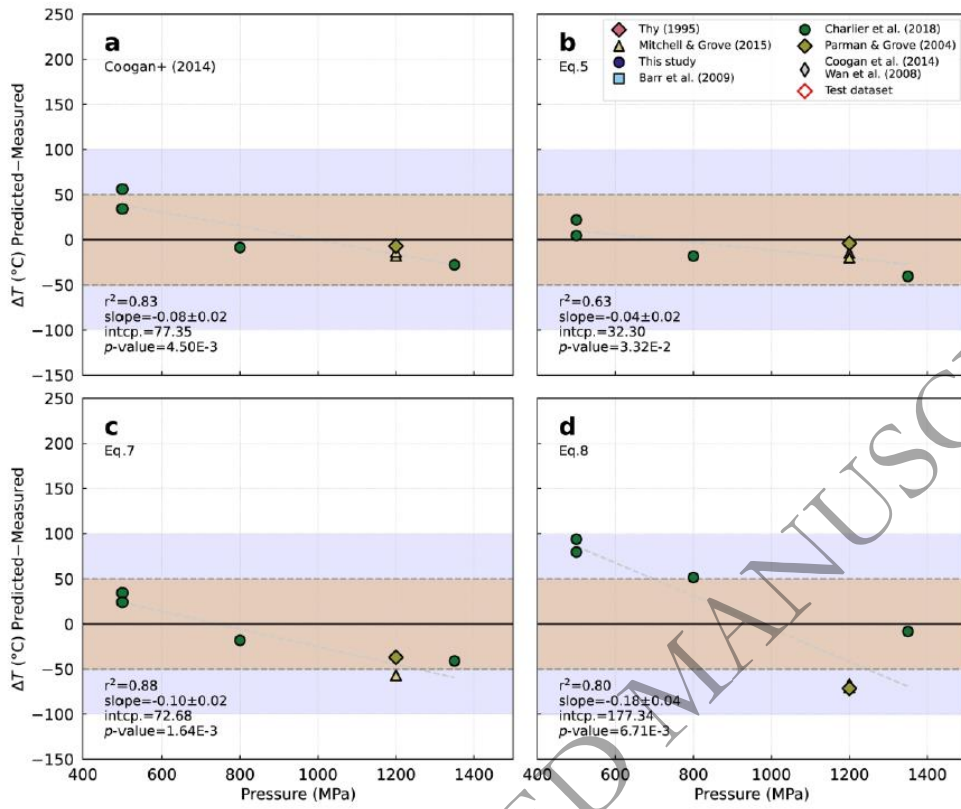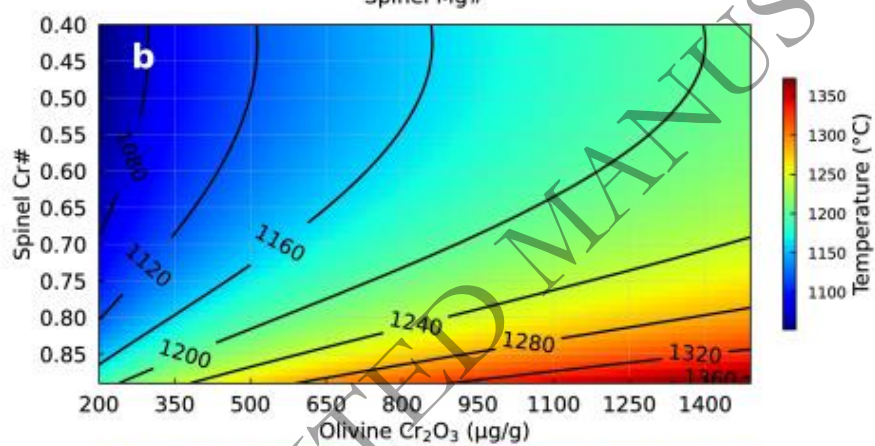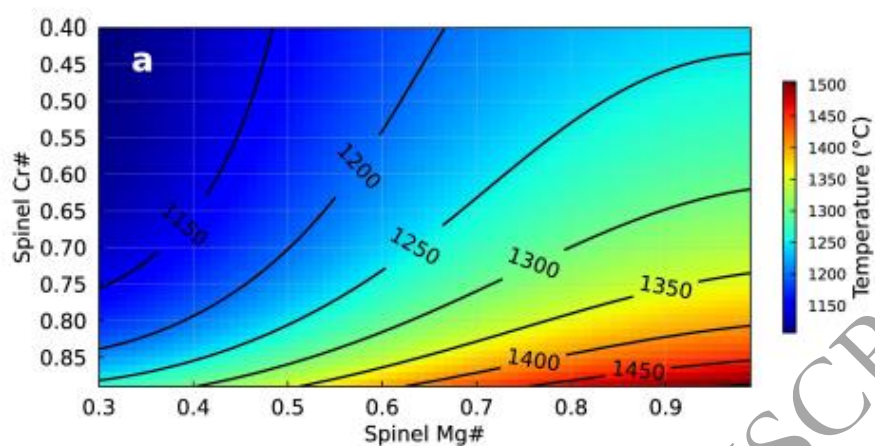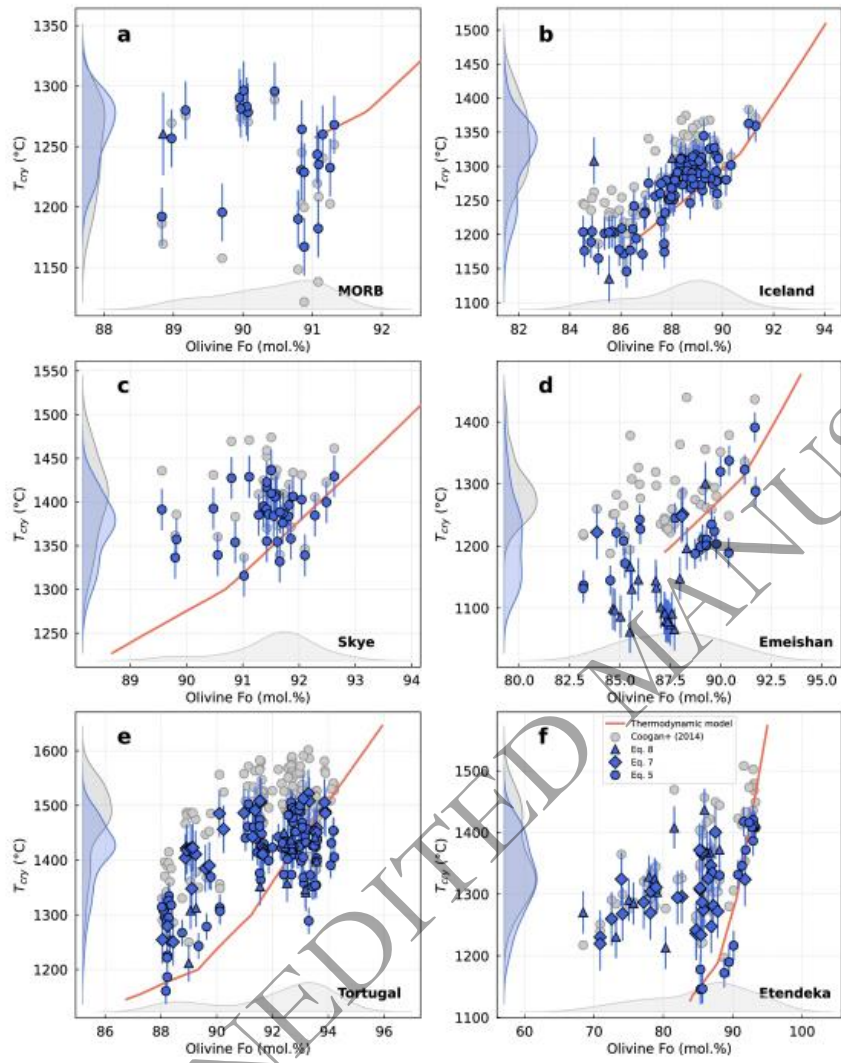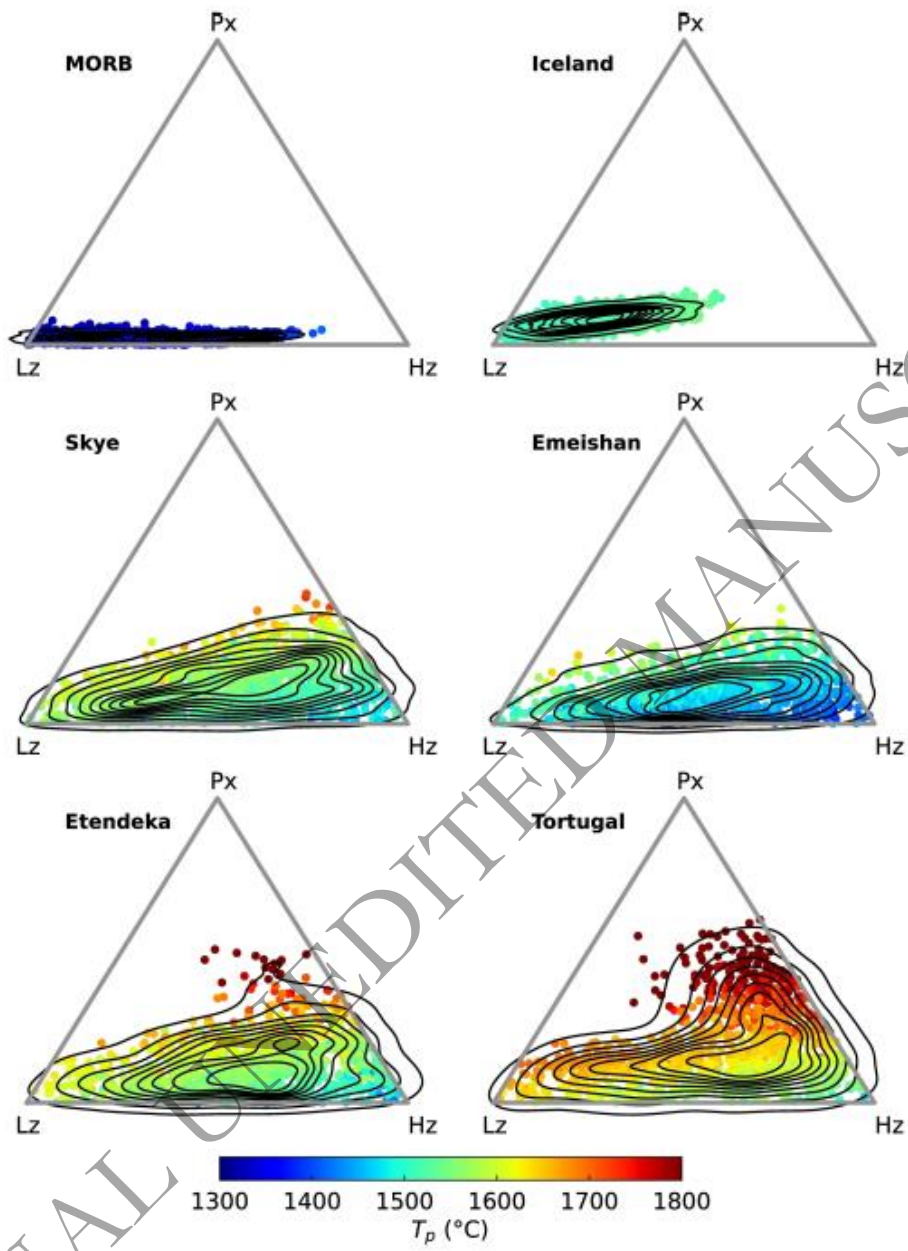1474
1475
1476
1477
1478
1479
1480

58

f11

1481
1482
1483
1484
1485
1486
1487
1488
1489
1490
1491
1492
1493

MORB

Iceland

Skye

Emeishan

Etendeka

Tortugal

T_p (°C)

f12

1494
1495
1496
1497
1498

f13
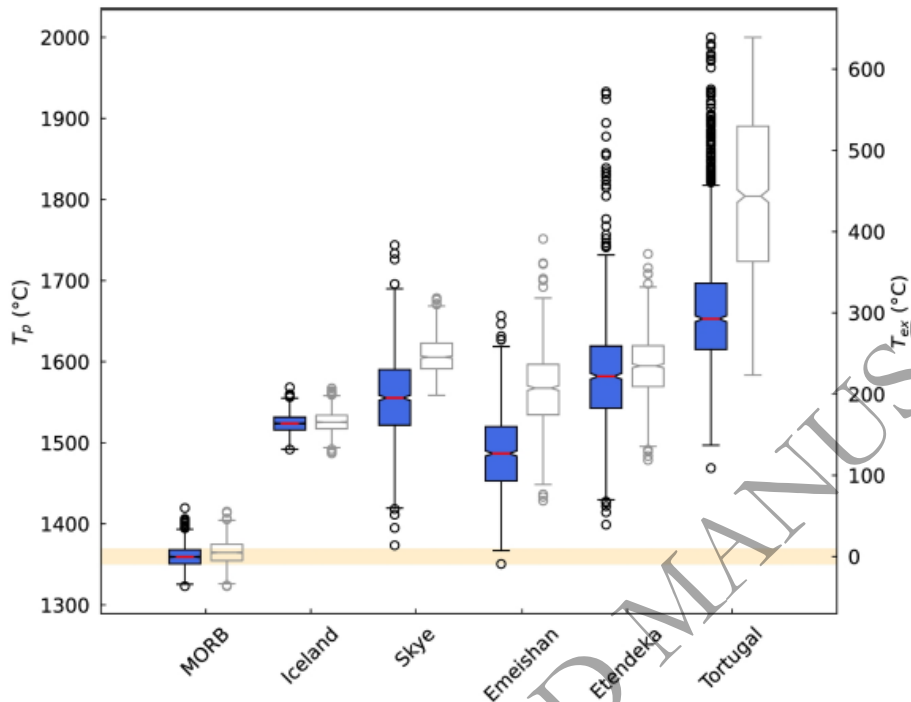
1499
1500

1501   Table. 1. Starting compositions used in this study.

Sample Name	Index[a]	SiO$_2$	TiO$_2$	Al$_2$O$_3$	FeO$_t$	MnO	MgO	CaO	Na$_2$O	K$_2$O	P$_2$O$_5$	Cr$_2$O$_3$	Sum
natural rocks													
Ny17-135	A	40.53	1.33	6.91	12.21	0.18	28.14	8.18	1.03	0.70	0.44	0.35	100.00
Ny17-135_Cr2*	B	37.95	1.24	6.47	11.43	0.17	31.08	7.66	0.96	0.66	0.41	1.97	100.00
Ny17-161_Cr	C	39.67	3.19	10.61	11.50	0.22	10.99	16.30	3.01	2.97	1.48	0.06	100.00
Ny17-161_Cr2	D	39.11	3.14	10.46	11.34	0.21	10.84	16.07	2.97	2.93	1.46	1.48	100.00
NYAM_Cr2*	E	41.88	1.12	4.34	12.03	0.07	31.08	6.23	0.50	0.65	0.14	1.98	100.00
Os82	F	50.21	0.70	16.33	9.39	0.15	10.23	10.29	2.18	0.33	0.09	0.09	100.00
Os82_Cr	G	49.52	0.69	16.11	9.26	0.15	10.09	10.15	2.15	0.33	0.09	1.46	100.00
PI-052_Cr2*	H	39.42	0.86	4.35	7.39	0.12	32.93	12.68	0.10	0.11	0.06	1.98	100.00
TO1	I	44.77	0.79	3.94	11.88	0.17	32.86	4.82	0.12	0.05	0.19	0.42	100.00
TO1_Cr	J	44.62	0.79	3.93	11.84	0.17	32.74	4.80	0.12	0.05	0.19	0.78	100.00
TO1_Cr2	K	44.07	0.78	3.88	11.69	0.17	32.34	4.74	0.12	0.05	0.19	1.98	100.00
TO2	L	45.18	0.89	4.48	11.84	0.17	31.35	5.18	0.14	0.18	0.20	0.41	100.00
TO2_Cr	M	45.01	0.88	4.46	11.80	0.17	31.23	5.16	0.14	0.18	0.20	0.79	100.00
TO2_Cr2	N	44.46	0.87	4.41	11.66	0.17	30.85	5.10	0.14	0.18	0.20	1.98	100.00
synthetic material													
TO1_syn_Cr1	O	45.89	0.74	3.84	10.22	0.20	31.91	4.66	0.15	1.08	0.16	1.00	100.00
TO1_syn_Cr2	P	45.44	0.73	3.80	10.12	0.19	31.60	4.62	0.15	1.06	0.16	1.98	100.00
TO2_syn_Cr1	Q	43.73	2.26	4.86	11.60	0.24	34.87	0.56	0.22	0.20	0.21	1.00	100.00
TO2_syn_Cr2	R	43.30	2.23	4.81	11.49	0.24	34.52	0.56	0.22	0.20	0.21	1.98	100.00
Ny17_syn_Cr1	S	38.42	1.26	6.53	10.40	0.24	32.07	7.74	0.99	0.68	0.43	1.00	100.00
Ny17_syn_Cr2	T	38.04	1.25	6.47	10.30	0.24	31.75	7.66	0.98	0.67	0.43	1.98	100.00
2Cr'+1Cr	U	45.01	0.84	9.69	12.31	0.10	22.71	7.67	1.00	0.04	0.11	0.52	100.00

1502   [a] Indexes are used to indicate which starting composition was used during the experiments
1503   in Table. 2.
1504   * Indicates starting composition was doped with forsterite or MgO to increase liquidus.
1505

Table. 2. Experimental conditions of extended, re-measured and literature data.

Run No.	Reference	T (°C)	Pressure (MPa)	log$f$O$_2$	ΔQFM	H2O (wt%)	Duration (h)
This study							
CAG03-K[a, b]	This study	1606.00	0.10	-4.53	0.00	0.00	7.00
CAG03-N[a]	This study	1606.00	0.10	-4.53	0.00	0.00	7.00
CAG03-H[a]	This study	1606.00	0.10	-4.53	0.00	0.00	7.00
CAG04-N[a]	This study	1568.00	0.10	-4.83	0.00	0.00	7.00
CAG04-E[a]	This study	1568.00	0.10	-4.83	0.00	0.00	7.00
CAG05-R[a]	This study	1571.00	0.10	-4.81	0.00	0.00	24.00
CAG05-S[a]	This study	1571.00	0.10	-4.81	0.00	0.00	24.00
CAG06-P[a]	This study	1571.00	0.10	-4.81	0.00	0.00	24.00
CAG06-R[a]	This study	1571.00	0.10	-4.81	0.00	0.00	24.00
CAG06-T[a]	This study	1571.00	0.10	-4.81	0.00	0.00	24.00
CAG07-T[a]	This study	1600.00	0.10	-4.58	0.00	0.00	24.00
NAB01-C	This study	1190.00	0.10	-8.53	0.00	0.00	72.00
NAB01-G	This study	1190.00	0.10	-8.53	0.00	0.00	72.00
NAB01-F	This study	1190.00	0.10	-8.53	0.00	0.00	72.00
NAB02-D	This study	1174.00	0.10	-8.72	0.00	0.00	94.00
NAB02-G	This study	1174.00	0.10	-8.72	0.00	0.00	94.00
NAB02-F	This study	1174.00	0.10	-8.72	0.00	0.00	94.00
NAB21-A	This study	1450.00	0.10	-5.84	0.00	0.00	24.00
NAB24-I	This study	1401.00	0.10	-6.29	0.00	0.00	72.00
NAB24-L	This study	1401.00	0.10	-6.29	0.00	0.00	72.00
NAB31-L	This study	1401.00	0.10	-4.29	2.00	0.00	48.00
NAB31-A	This study	1401.00	0.10	-4.29	2.00	0.00	48.00
NAB41-J	This study	1469.00	0.10	-5.67	0.00	0.00	48.00
NAB41-M	This study	1469.00	0.10	-5.67	0.00	0.00	48.00
NAB45-K[a, c]	This study	1529.00	0.10	-5.15	0.00	0.00	24.00
NAB45-N[a, c]	This study	1529.00	0.10	-5.15	0.00	0.00	24.00
NAB45-B[a, c]	This study	1529.00	0.10	-5.15	0.00	0.00	24.00
NAB45-H[a, c]	This study	1529.00	0.10	-5.15	0.00	0.00	24.00
NAB49-Q	This study	1500.00	0.10	-5.40	0.00	0.00	24.00
NAB49-R	This study	1500.00	0.10	-5.40	0.00	0.00	24.00
NAB51-R	This study	1500.00	0.10	-5.40	0.00	0.00	24.00
NAB51-S	This study	1500.00	0.10	-5.40	0.00	0.00	24.00
NAB52-R[a]	This study	1529.00	0.10	-5.15	0.00	0.00	24.00
NAB53-O	This study	1445.00	0.10	-5.89	0.00	0.00	72.00
NAB53-Q	This study	1445.00	0.10	-5.89	0.00	0.00	72.00

63

NAB53-R	This study	1445.00	0.10	-5.89	0.00	0.00	72.00
NAB53-S	This study	1445.00	0.10	-5.89	0.00	0.00	72.00
NAB57-R[a]	This study	1530.00	0.10	-5.15	0.00	0.00	24.00
NAB57-T[a]	This study	1530.00	0.10	-5.15	0.00	0.00	24.00
NAB58-R	This study	1397.00	0.10	-6.33	0.00	0.00	72.00
*NAB88-R	This study	1350.00	0.10	-8.39	-1.60	0.00	118.00
NAB89-U	This study	1253.00	0.10	-9.41	-1.60	0.00	120.00
*NAB89-R	This study	1253.00	0.10	-9.41	-1.60	0.00	120.00
NAB90-U	This study	1305.00	0.10	-8.85	-1.60	0.00	36.00
*NAB91-Q	This study	1305.00	0.10	-8.85	-1.60	0.00	36.00
*NAB91-R	This study	1305.00	0.10	-8.85	-1.60	0.00	36.00
Re-analyzed experiments			0.00				
com1-12	Barr et al. (2009)	1320.00	0.10	-7.09	0.00	0.00	
com1-2	Barr et al. (2009)	1350.00	0.10	-6.79	0.00	0.00	
com1-4	Barr et al. (2009)	1300.00	0.10	-7.30	0.00	0.00	
213.00	Thy (1995)	1240.00	0.10	-7.95	0.00	0.00	
214.00	Thy (1995)	1251.00	0.10	-7.83	0.00	0.00	
215.00	Thy (1995)	1231.00	0.10	-8.05	0.00	0.00	
216.00	Thy (1995)	1221.00	0.10	-8.17	0.00	0.00	
218.00	Thy (1995)	1200.00	0.10	-8.41	0.00	0.00	
224.00	Thy (1995)	1260.00	0.10	-7.73	0.00	0.00	
228.00	Thy (1995)	1279.00	0.10	-7.52	0.00	0.00	
230.00	Thy (1995)	1300.00	0.10	-7.30	0.00	0.00	
233.00	Thy (1995)	1311.00	0.10	-7.18	0.00	0.00	
234.00	Thy (1995)	1320.00	0.10	-7.09	0.00	0.00	
235.00	Thy (1995)	1328.00	0.10	-7.01	0.00	0.00	
c553	Mitchell & Grove (2015)	1215.00	1200.00	-8.78	-0.54	6.00	
c559	Mitchell & Grove (2015)	1250.00	1200.00	-8.42	-0.59	3.70	
on66-ha04	Charlier et al. (2018)	1230.00	500.00	-10.58	-2.52	0.00	
twm-f0.6-b1255	Charlier et al. (2018)	1360.00	1350.00	-9.03	-2.34	0.00	
twm71-b1295	Charlier et al. (2018)	1300.00	800.00	-9.72	-2.42	0.00	
twm71-ha04	Charlier et al. (2018)	1230.00	500.00	-10.58	-2.52	0.00	
w7	Parman & Grove (2004)	1320.00	1200.00	-8.09	-1.00	7.40	
Literature data							
w39	Wan et al. (2008)	1250.00	0.10	-9.55	-1.71	0.00	
w83_1	Wan et al. (2008)	1250.00	0.10	-9.55	-1.71	0.00	
w83_2	Wan et al. (2008)	1250.00	0.10	-9.55	-1.71	0.00	
w83_3	Wan et al. (2008)	1250.00	0.10	-9.55	-1.71	0.00	

64

w83_4	Wan et al. (2008)	1250.00	0.10	-9.55	-1.71	0.00
w83_5	Wan et al. (2008)	1250.00	0.10	-9.55	-1.71	0.00
w83_6	Wan et al. (2008)	1250.00	0.10	-9.55	-1.71	0.00
w83_7	Wan et al. (2008)	1250.00	0.10	-9.55	-1.71	0.00
w35	Wan et al. (2008)	1300.00	0.10	-8.95	-1.65	0.00
w71_1	Wan et al. (2008)	1300.00	0.10	-8.95	-1.65	0.00
w71_2	Wan et al. (2008)	1300.00	0.10	-8.95	-1.65	0.00
w72_1	Wan et al. (2008)	1300.00	0.10	-8.95	-1.65	0.00
w72_2	Wan et al. (2008)	1300.00	0.10	-8.95	-1.65	0.00
w73	Wan et al. (2008)	1300.00	0.10	-8.95	-1.65	0.00
w36_1	Wan et al. (2008)	1350.00	0.10	-8.35	-1.56	0.00
w36_2	Wan et al. (2008)	1350.00	0.10	-8.35	-1.56	0.00
w55	Wan et al. (2008)	1350.00	0.10	-8.35	-1.56	0.00
w55_1	Wan et al. (2008)	1350.00	0.10	-8.35	-1.56	0.00
w55_2	Wan et al. (2008)	1350.00	0.10	-8.35	-1.56	0.00
w62_1	Wan et al. (2008)	1350.00	0.10	-8.35	-1.56	0.00
w62_2	Wan et al. (2008)	1350.00	0.10	-8.35	-1.56	0.00
w66	Wan et al. (2008)	1350.00	0.10	-8.35	-1.56	0.00
w66_1	Wan et al. (2008)	1350.00	0.10	-8.35	-1.56	0.00
w61	Wan et al. (2008)	1400.00	0.10	-7.85	-1.55	0.00
w61_1	Wan et al. (2008)	1400.00	0.10	-7.85	-1.55	0.00
w86	Wan et al. (2008)	1400.00	0.10	-7.85	-1.55	0.00
w86_1	Wan et al. (2008)	1400.00	0.10	-7.85	-1.55	0.00
w86_2	Wan et al. (2008)	1400.00	0.10	-7.85	-1.55	0.00
w60_1	Wan et al. (2008)	1450.00	0.10	-7.35	-1.51	0.00
w60_2	Wan et al. (2008)	1450.00	0.10	-7.35	-1.51	0.00
w78	Wan et al. (2008)	1450.00	0.10	-7.35	-1.51	0.00
w328*	Coogan et al. (2014)	1250.00	0.10	-0.68	7.16	0.00
w328*_1	Coogan et al. (2014)	1250.00	0.10	-0.68	7.16	0.00
w290_1	Coogan et al. (2014)	1350.00	0.10	-0.68	6.11	0.00
w330	Coogan et al. (2014)	1350.00	0.10	-0.68	0.49	0.00
w330_1	Coogan et al. (2014)	1350.00	0.10	-6.30	0.49	0.00
w330_2	Coogan et al. (2014)	1350.00	0.10	-6.30	0.49	0.00
w332	Coogan et al. (2014)	1350.00	0.10	-7.30	-0.51	0.00
w332_1	Coogan et al. (2014)	1350.00	0.10	-7.30	-0.51	0.00
w338	Coogan et al. (2014)	1350.00	0.10	-5.50	1.29	0.00
matzen2011_15	Matzen et al. (2011)	1349.00	0.10	-6.87	-0.07	0.00
matzen2011_6	Matzen et al. (2011)	1302.0	0.10	-7.36	-0.08	0.00

65

		0				
matzen2011_8	Matzen et al. (2011)	1302.00	0.10	-7.36	-0.08	0.00
matzen2011_46	Matzen et al. (2011)	1300.00	0.10	-7.41	-0.11	0.00
H&J_1998_FAD1b	Hanson & Jones (1998)	1320.00	0.10	-3.00	4.09	0.00
H&J_1998_FAD2	Hanson & Jones (1998)	1320.00	0.10	-3.00	4.09	0.00
H&J_1998_FAD3	Hanson & Jones (1998)	1320.00	0.10	-3.00	4.09	0.00
H&J_1998_FAS1	Hanson & Jones (1998)	1320.00	0.10	-3.00	4.09	0.00
H&J_1998_FAS1_1	Hanson & Jones (1998)	1320.00	0.10	-3.00	4.09	0.00

1506 [a] indicates 1–2 hour thermal oscillation (±10°C) was applied;
1507 [b] Experiment number ends with the starting composition noted in Table. 1;
1508 [c] indicates chromite seeds were applied.
1509 * indicates experiments contain clinopyroxene
1510

ORIGINAL UNEDITED MANUSCRIPT

1511 Table. 3. Scenarios for selecting the appropriate model for OSAT.

Scenarios	Model selection
Compare 3 models (Eq. 5, Eq. 7 & Eq. 8)	
S1: T_Eq5 > T_Eq7, T_Eq5 > T_Eq8	Eq.5
If not S1, apply Z-test:	
Z_(Eq5&Eq7) > Z_(Eq5&Eq8) > 1.35	Eq.7
Z_(Eq5&Eq8) > Z_(Eq5&Eq7) > 1.35	Eq.8
Z_(Eq5&Eq8)< 1.35, Z_(Eq5&Eq7) < 1.35	Eq.5
Z_(Eq5&Eq7) > 1.35 > Z_(Eq5&Eq8)	Eq.7
Z_(Eq5&Eq8) > 1.35 > Z_(Eq5&Eq7)	Eq.8
Compare 2 models (Eq. 5 & Eq. 7)	
S2: T_Eq5 > T_Eq7	Eq.5
If not S2, apply Z-test:	
Z_(Eq5&Eq7) > 1.35	Eq.7
Z_(Eq5&Eq7) < 1.35	Eq.5

1512
1513
1514

Table. 4. Comparison of the temperature estimates of models.

Location	observations	Eq. 5		Eq. 7		Eq. 8		Model of Coogan et al. (2014)	
		Min-Max (°C)	T_{cry} (°C)[a]	Min-Max (°C)	T_{cry} (°C)	Min-Max (°C)	T_{cry} (°C)	Min-Max (°C)	T_{cry} (°C)
MORB (Siqueiros)	22	1167-1296	1250^{+4}_{-7}	1096-1260	1197^{+6}_{-8}	1115-1278	1218^{+5}_{-8}	1121-1292	1230^{+59}_{-91}
Iceland	85	1145-1362	1274^{+5}_{-1}	1112-1350	1247^{+8}_{-8}	1169-1345	1264^{+6}_{-6}	1183-1383	1283^{+84}_{-66}
Skye	35	1315-1436	1388^{+4}_{-5}	1290-1425	1348^{+4}_{-4}	1307-1436	1376^{+5}_{-5}	1337-1474	1409^{+60}_{-65}
Emeishan	48	1131-1391	1202^{+1}_{-6}	1061-1361	1145^{+1}_{-6}	1166-1397	1238^{+9}_{-4}	1188-1439	1271^{+10}_{-55}
Etendeka	62	926-1420	1178^{+2}_{-1}	1157-1447	1268^{+1}_{-9}	1178-1455	1295^{+1}_{-8}	1197-1508	1323^{+15}_{-10}
Tortugal	157	1109-1506	1405^{+8}_{-1}	1191-1471	1389^{+6}_{-1}	1217-1522	1426^{+7}_{-1}	1250-1601	1492^{+89}_{-17}

1515 [a] T_{cry} is reported as median value with 95th and 5th percentile quoted.
1516

1517 Table. 5. Summary of the posterior distributions of the T_p, ϕ_{Px}, ϕ_{Hz} in the inversion model as a comparison with
1518 the results from Matthews et al. (2021).

Location	T_{cry} (°C)[a]	This study			Matthews et al. (2021)		
		T_p (°C)	Φ_{Px}	Φ_{Hz}	T_p (°C)	Φ_{Px}	Φ_{Hz}
MORB	1266±22	1355^{+24}_{-19}	$0.02^{+0.02}_{-0.02}$	$0.34^{+0.25}_{-0.30}$	1364^{+18}_{-23}	$0.02^{+0.02}_{-0.02}$	$0.40^{+0.16}_{-0.37}$
Iceland	1363±24	1518^{+21}_{-17}	$0.08^{+0.04}_{-0.04}$	$0.23^{+0.18}_{-0.17}$	1525^{+21}_{-18}	$0.08^{+0.05}_{-0.04}$	$0.27^{+0.16}_{-0.20}$
Skye	1436±24	1550^{+80}_{-82}	$0.12^{+0.16}_{-0.10}$	$0.51^{+0.32}_{-0.39}$	1566^{+73}_{-70}	$0.10^{+0.15}_{-0.10}$	$0.47^{+0.28}_{-0.39}$
Emeishan	1391±24	1481^{+87}_{-78}	$0.10^{+0.14}_{-0.09}$	$0.53^{+0.29}_{-0.36}$	1555^{+100}_{-97}	$0.13^{+0.14}_{-0.10}$	$0.55^{+0.31}_{-0.38}$
Etendeka	1447±34	1577^{+106}_{-98}	$0.11^{+0.19}_{-0.10}$	$0.53^{+0.31}_{-0.38}$	1599^{+104}_{-79}	$0.10^{+0.15}_{-0.09}$	$0.51^{+0.32}_{-0.38}$
Tortugal	1506±24	1648^{+193}_{-91}	$0.15^{+0.29}_{-0.13}$	$0.50^{+0.31}_{-0.38}$	1813^{+157}_{-149}	$0.29^{+0.18}_{-0.24}$	$0.45^{+0.32}_{-0.27}$

1519 [a] Crystallization temperature used in the inversion model.
1520

Table. A1. Independent compositional, ordering variables and definitions of site mole fractions

$$X_2 = X_{Mg^{2+}}^{TET} + 2X_{Mg^{2+}}^{OCT}$$

$$X_{Mg^{2+}}^{TET} = \frac{X_2 + s_1}{2}$$

$$X_3 = X_{Cr^{3+}}^{TET} + X_{Cr^{3+}}^{OCT}$$

$$X_{Fe^{2+}}^{TET} = X_4 + s_2 + s_3 + s_4 - \frac{X_2 + s_1}{2}$$

$$X_4 = 2X_{Ti^{4+}}^{OCT}$$

$$X_{Fe^{3+}}^{TET} = X_5 - s_4$$

$$X_5 = X_{Fe^{3+}}^{TET} + 2X_{Fe^{3+}}^{OCT}$$

$$X_{Al^{3+}}^{TET} = 1 - X_3 - X_4 - X_5 - s_2$$

$$s_1 = X_{Mg^{2+}}^{TET} - 2X_{Mg^{2+}}^{OCT}$$

$$X_{Cr^{3+}}^{TET} = X_3 - s_3$$

$$s_2 = \frac{2X_{Al^{3+}}^{OCT} - X_{Al^{3+}}^{TET}}{2}$$

$$X_{Mg^{2+}}^{OCT} = \frac{X_2 - s_1}{4}$$

$$s_3 = \frac{2X_{Cr^{3+}}^{OCT} - X_{Cr^{3+}}^{TET}}{2}$$

$$X_{Fe^{2+}}^{OCT} = \frac{1 - s_2 - s_3 - s_4}{2} - \frac{X_2 - s_1}{4}$$

$$s_4 = \frac{2X_{Fe^{3+}}^{OCT} - X_{Fe^{3+}}^{TET}}{2}$$

$$X_{Fe^{3+}}^{OCT} = \frac{X_5 + s_4}{2}$$

$$X_{Fe^{2+}}^{TET} + X_{Fe^{2+}}^{TET} + X_{Al^{3+}}^{TET} + X_{Cr^{3+}}^{TET} + X_{Fe^{3+}}^{TET} = 1$$

$$X_{Al^{3+}}^{OCT} = \frac{1 - X_3 - X_4 - X_5 + s_2}{2}$$

$$X_{Fe^{2+}}^{OCT} + X_{Mg^2}^{OCT} + X_{Al^{3+}}^{OCT} + X_{Cr^{3+}}^{OCT} + X_{Fe^{3+}}^{OCT} + X_{Ti^{4+}}^{OCT} = 1$$

$$X_{Cr^{3+}}^{OCT} = \frac{X_3 + s_3}{2}$$

$$X_{Ti^{4+}}^{OCT} = \frac{X_4}{2}$$

1521
1522
1523
1524

1525 **Table. A2.** Coefficients and statistical parameters of regressions for OSAT.

	Coefficients[a]	Statistical parameters	
		Eq. 5	
c0	-0.168	r^2	0.97
c1	1.487	SEE	20.20
c2	-0.593	RMSE	29.00
c3	-0.630	*p*-value	1.11E-16
c4	0.390	r^2_{MCCV}	0.97
c5	0.009	SEE_{MCCV}	20.20
c6	-2.492	$RMSE_{MCCV}$	23.90
c7	0.065		
c8	-0.031		
c9	-4.141		
c10	-0.428		
c11	-4.637		
c12	-0.054		
c13	-10.803		
c14	2.714		
b	0.654		
		Eq. 7	
Cr#	1.144(0.136)	r^2	0.83
$lnK_{D_{Al}}$	-0.865(0.046)	SEE	44.80
const	0.740(0.317)	RMSE	34.40
		p-value	2.88E-36
		r^2_{MCCV}	42.10
		SEE_{MCCV}	0.92
		$RMSE_{MCCV}$	43.30
		Eq. 8	
Cr#	0.543(0.121)	r^2	0.91
$lnK_{D_{Al}}$	-0.657(0.040)	SEE	31.70
$lnK_{D_{Cr}}$	-0.389(0.041)	RMSE	39.10
const	0.049(0.241)	*p*-value	3.79E-47
		r^2_{MCCV}	0.94
		SEE_{MCCV}	35.80
		$RMSE_{MCCV}$	34.20

1526 [a] number in bracket indicates the 1σ error of coefficients
1527 for the linear regression.
1528